

# Thermionic Emission Studies from laser-heated CVD diamond incorporating Li, B co- dopants

---

Peter Arthur Cassell

4/28/2014

Chemical Physics MSc 30 Credit Point Project

## *Abstract*

Laser-heated thermionic emission was trialled experimentally for the first time at Bristol University Diamond Laboratory. 1cmx1cm Diamond and molybdenum samples were heated by 40W radiation from a carbon dioxide laser in order to determine the maximum cathode temperatures that could be reached by the thermionic setup. Freestanding boron-doped diamond (BDD) reached the highest temperature of  $799\pm 5^\circ\text{C}$ . Enhanced absorption Mo samples reached  $681\pm 5^\circ\text{C}$ . The laser-heated thermionic emission measurements for lithium diffused, hydrogen terminated BDD gave an emission peak of  $22.2\pm 0.05 \mu\text{A cm}^{-2}$  and hydrogen terminated BDD without lithium diffusion gave an emission peak of  $11.2\pm 0.05 \mu\text{A cm}^{-2}$ . These results are in agreement with literature; confirming the benefit of lithium diffusion upon the thermionic emission from BDD.

# 1 Contents

2	Project Introduction .....	2
3	Literature Review .....	2
3.1	Semiconductor Basics .....	2
3.1.1	Doping.....	3
3.2	Thermionic Emissions Basics .....	4
3.2.1	Thermionic Energy Converters (TECs) .....	6
3.2.2	Photo-Enhanced Thermionic Emission (PETE).....	8
3.2.3	Common Thermionic Emitting Devices .....	9
3.2.4	Diamond as a Thermionic Emitter .....	10
3.2.5	Doping of Diamond .....	11
3.2.6	Modifying the diamond surface for NEA .....	15
3.2.7	Li, LiO terminations and computational analysis of diamond surface structure .....	19
3.3	Radiation conversion and transport in diamond. Role of bulk and surface defects. ....	21
3.4	Absorption, Plasmons and Heat transport .....	23
3.5	A Note on the manufacture of CVD Diamond .....	25
3.6	Diamond potential for Photo-Enhanced Thermionic Emission (PETE) .....	27
4	Experimental .....	27
4.1.1	Initial Setup .....	27
4.1.2	Samples Used .....	27
4.2	Optimising the Thermionic Emission Set-up .....	28
4.2.1	Mounting the diamond sample.....	28
4.2.2	Enhancing the Absorption of the Molybdenum Plate .....	29
4.3	Heating Tests.....	31
4.4	Thermionic Measurements .....	32
4.5	Results and Discussion .....	33
4.6	Conclusion.....	36
4.7	Acknowledgements.....	36
5	Bibliography.....	36
6	Appendix .....	40

## 2 Project Introduction

Diamond is an excellent candidate for low-temperature thermionic emission due to its chemically stable surface, capability for surface modification for negative electron affinity and high thermal conductivity. This thesis reviews the field of thermionic emission and the place of diamond within the field as well as reporting on the experimental work carried out at Bristol University Diamond Laboratory to achieve thermionic emission from boron doped diamond using laser heating methods and determine the parameters which are significant to the thermionic emission from the diamond surface.

Previous tests at Bristol University Diamond Group have been carried out using electrically heated diamond to generate thermionic emission however the electric heater inconvenient to incorporate into the thermionic setup and escaped current from the electric heater may interfere with the thermionic emission current measurements. Laser heating provides a distinct advantage in that the heating source need not be in close proximity with the thermionic cathode so does not interfere with thermionic emission measurements. Laser heating also only heats targeted areas and energy absorption at the cathode surface can be optimized. A new 40W CO<sub>2</sub> laser with wavelength of 10.6μm was acquired for this project.

The literature review covers the theory of thermionic electron emission, a review of conventional electrode materials and their properties, properties of diamond and the use of dopants to produce semiconductivity, radiation conversion in diamond, transport in diamond and the role of surface modification upon thermionic emission current.

## 3 Literature Review

### 3.1 Semiconductor Basics

Materials that exhibit semiconducting properties have full electronic bands and a small enough band gap between the valence band and the conduction band that electrons may be thermally excited to the conduction band leaving a hole in the conduction band (see Figure 1).

The number of electrons promoted to the conduction band of the semiconductor is proportional to the Boltzmann factor,  $e^{\frac{-E_g}{k_B T}}$ .

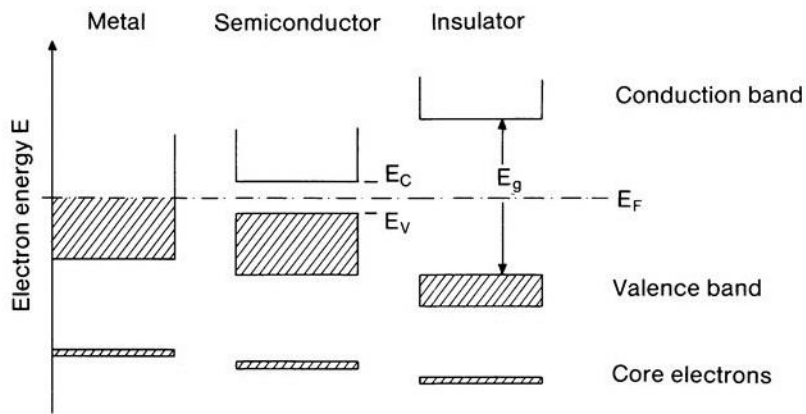


Figure 1 - The Band Structures of Metals, Semiconductors and Insulators (Ibach and Luth 12.1) [1]

The size of the band gap,  $E_g$ , is temperature dependent because the band gap is related to the lattice parameter,  $a$ , which increases with the thermal expansion of the lattice structure. The relationship between band gap and temperature is defined by the Varshni equation.

$$E_g(T) = E_g(0) - \frac{\alpha_g T^2}{T + \beta_g} \quad \text{Equation 1- Varshni Equation [2] [1]}$$

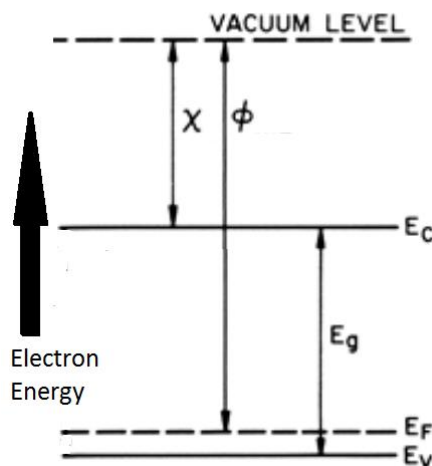


Figure 2 - A basic p-type semiconductor showing band gap  $E_g$  as the energy difference between the conduction band  $E_c$  and the valence band  $E_v$ .

The electron affinity,  $\chi$ , is defined as the energy difference between the conduction band and the vacuum level. In the majority of semiconductors, the electron affinity is positive however some semiconductors can be modified such that the energy of the conduction band is higher than that of the vacuum level, as such the material has a negative electron affinity (NEA).

The work function,  $\phi$ , is defined as the energy difference between the Fermi level,  $E_F$ , and the vacuum level. The work function of a material is a surface dependent property. The surface can be modified and thus the work function can be changed.

### 3.1.1 Doping

The electrical activity of the semiconductor can be increased by the introduction of dopants into the material which provide either an additional electron ( $e^-$ ) or a hole ( $h^+$ ) to the material.

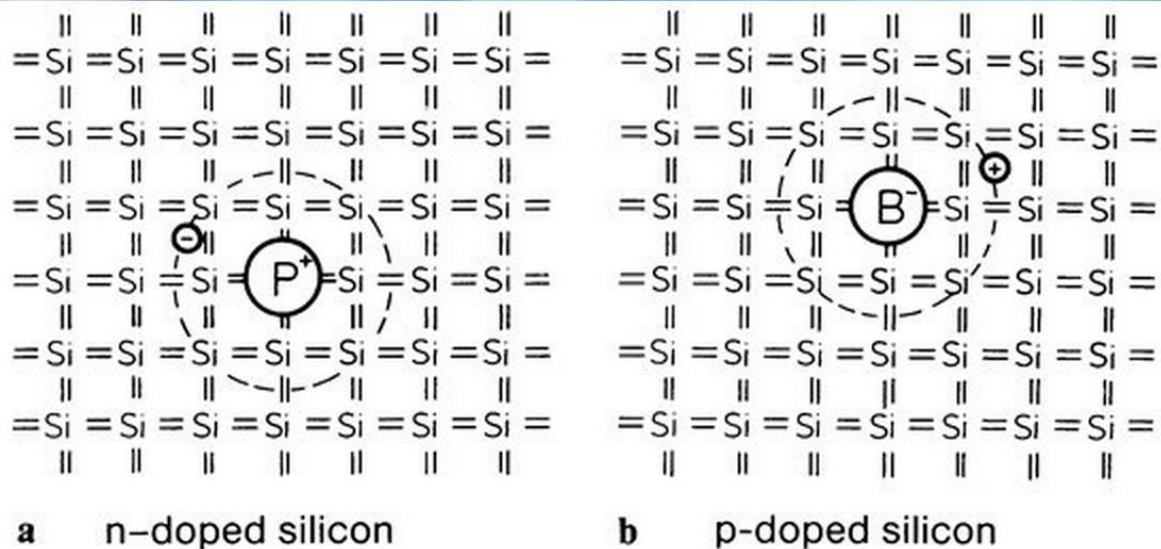


Figure 3 - The doping of a semiconductor. a) shows n-doped silicon with Phosphorous donor providing an additional electron to the lattice and b) shows p-doped silicon with Boron acceptor providing an additional hole to the lattice (Ibach and Luth 12.6) [1]

A donor dopant is an element which has one additional valence electron compared to the bulk of the semiconductor lattice. Silicon has a valence of four and phosphorous has a valence of five so when P forms four  $sp^3$  bonds with the four neighbouring Si atoms it will have a spare electron which can be considered to be an electron that is weakly bound to the P atom and can be removed from the donor for less energy cost than electrons in the valence band of Si. The donor electron sits occupies the donor energy level,  $E_D$ , which is just below the conduction level,  $E_C$ .

An acceptor dopant is an element which has one additional hole compared to the bulk of the semiconductor lattice. When Boron (trivalent) is introduced to a Silicon lattice, it does not have enough electrons to form all four  $sp^3$  bonds with the four surrounding Si atoms. This can be considered as if the B is able to bond but a hole has been added to the system. The hole occupies the acceptor energy level,  $E_A$ , which sits just above the valence level.

Crystal lattices can be defined in terms of their unit cells and their Brillouin Zones [3]. The band structure of a crystal lattice can be represented in reciprocal space (k space) and it is common that the energies of electrons and holes at particular points in the reciprocal lattice will have different energies.

### 3.2 Thermionic Emissions Basics

An electron in the valence band of a thermionic material can be thermally excited to the vacuum level, leaving a hole at top of the valence band. The likelihood of exciting an electron with sufficient energy to reach the vacuum level increases as the temperature of the material increases. The probability of an electron having enough energy to reach the vacuum level is higher for materials with a low work function.

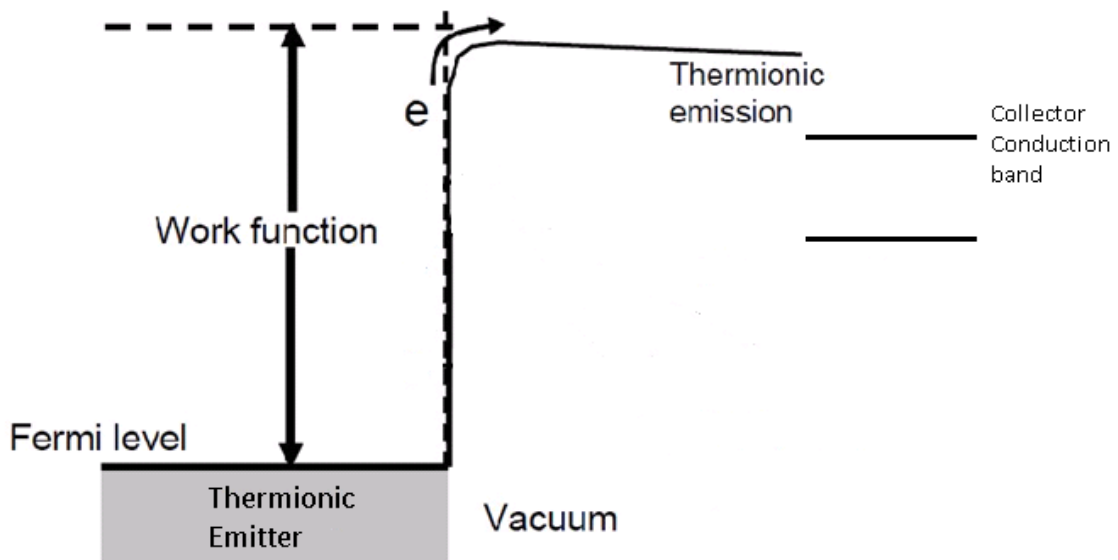


Figure 4 - Thermionic Emission of an electron into the vacuum level for a material with positive electron affinity.

Thermionic emission is more likely, and thus higher emission currents can be achieved from NEA material surfaces. Figure 4 and Figure 5 demonstrate the band energies which give rise to a positive electron affinity (PEA) and negative electron affinity (NEA) respectively.

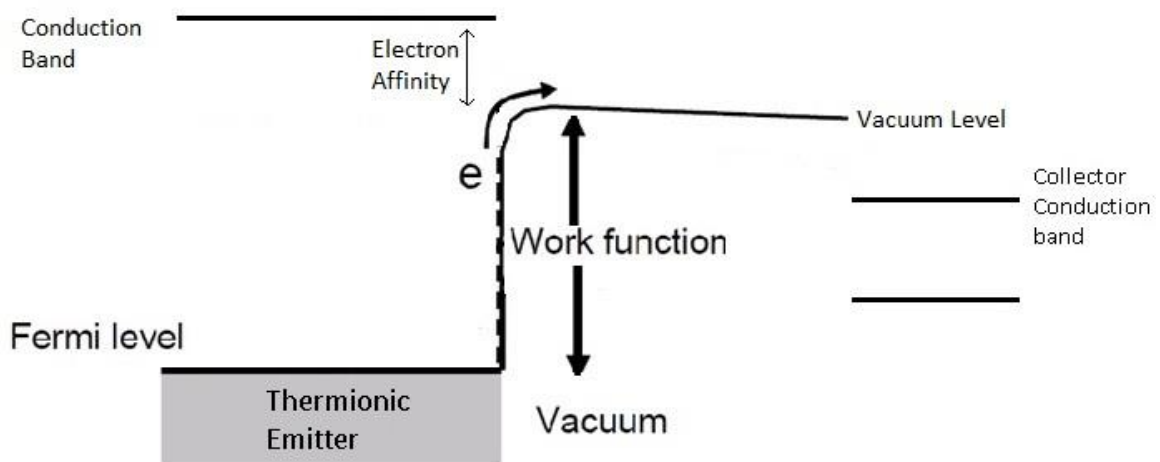


Figure 5 - An energy diagram of a thermionic emitter with negative electron affinity

The Richardson-Dushman equation is used to calculate the emitted current density from the cathode.

$$J(T) = AT^2 \exp\left(\frac{-e\phi_{eff}}{k_b T}\right) \quad \text{Equation 2 [4] [5] [6] [7]}$$

where  $A$  is the Richardson constant unique to each individual emitting material,  $T$  is the temperature of the cathode,  $e$  is the charge on an electron,  $\phi_{eff}$  is the effective work function and  $k_b$  is the Boltzmann constant. For tungsten, a typical thermionic emitter,  $A$ , has been determined to be approximately  $60 \text{ A cm}^{-2} \text{ K}^{-2}$  though this can be lowered to  $1.5 \text{ A cm}^{-2} \text{ K}^{-2}$  by lowering the work function of the material through introducing defects to the lattice [8]. The consequence of the

Richardson equation is that materials with a low work function and high Richardson constant are efficient thermionic emitters.

Escaping electrons (minority carriers) which are travelling through the depletion region may lose energy through scattering by lattice phonons and thus may recombine with holes in the vacuum level. Collisions with lattice phonons take place on timescales of the order  $10^{-12}$ s. [9] Minimising the effect of lattice phonons upon thermionic emission involves engineering a narrow depletion region by using high p-type dopant concentrations. Electrons may also become trapped in surface states, preventing their emission from the material. Recombination and electron trapping occur least often in perfect crystals (minimal defects) [9] so the quality of manufacture of the thermionic crystal affects the maximum possible efficiency of the device.

The lifetime of minority carriers in the crystal must be sufficient so that the carrier has time to escape the depletion region. The diffusion length in a semiconductor is the length that a carrier travels from its generation point to its recombination. It can be considered that the minority carrier diffusion length should be greater than the depth at which the electron has been excited in thermionic devices so that the electron can escape the material before recombination becomes a certainty. A typical carrier lifetime,  $\tau$ , is  $10^{-9}$ s to  $10^{-7}$ s. The minority carrier diffusion length,  $L$ , in a good quality NEA emitter can be up to  $5\mu\text{m}$ . [9]

When considering electron movement through the crystal lattice in a statistical manner it is helpful to consider the process in terms of the diffusion equation, the generation rate,  $G$ , and diffusion constant,  $D$ .  $G(x)$  is the position-dependent generation rate. This model holds for crystals considered in one dimension with an exterior electric field being applied and no temperature gradient (high thermal conductivity).  $n$  is the average number density of carriers leaving the surface for a material with hole density,  $p_0$ , electron and hole masses  $m_e$  and  $m_h$  at temperature  $T$ .

$$D \left( \frac{\delta^2 n}{\delta x^2} \right) - \frac{n(x)}{\tau} + G(x) = 0 \quad \text{Equation 3 [9]}$$

The diffusion equation essentially states that at any position,  $x$ , in the lattice, sum the generation rate of electrons, the diffusion rate of electrons minus the recombination rate of carriers is equal to zero. The solution of the differential equation has a number of useful mathematical applications.

Firstly, the number of electrons which are thermally excited to the conduction band can be deduced as:

$$n = \frac{4}{p_0} \left( \frac{2\pi k_B T}{h} \right)^3 (m_e m_h)^{\frac{3}{2}} e^{\left( \frac{-E_g}{k_B T} \right)} \quad \text{Equation 4 [9]}$$

For a NEA surface and assuming an escape probability of 0.5, the theoretical current emitted into the vacuum level using the diffusion equation is:

$$J_d = \frac{10^{31} T^3}{p_0} \left( \frac{m_e m_h}{m^2} \right)^{\frac{3}{2}} \frac{qD}{L} e^{\left( \frac{-E_g}{k_B T} \right)} \quad \text{Equation 5 [9]}$$

### 3.2.1 Thermionic Energy Converters (TECs)

In a Thermionic Energy Converter (TEC), the hot thermionic cathode emits electrons into the vacuum level which are then collected at the cooler anode. The TEC has uses no mechanical process to convert energy. [10]

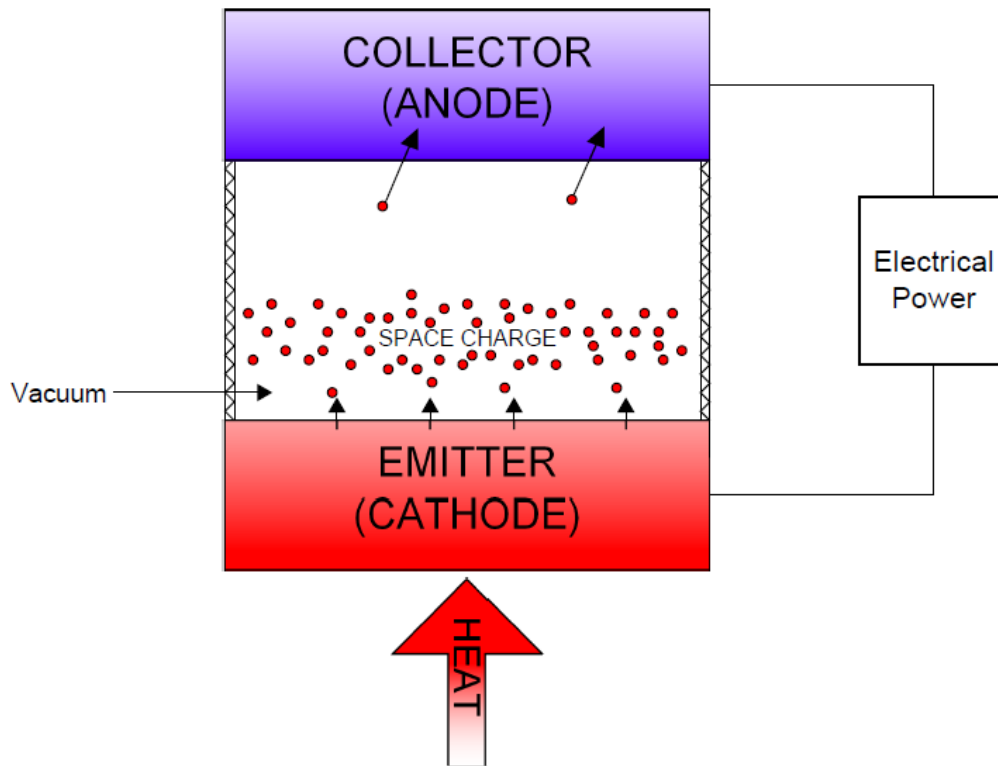


Figure 6 - A schematic diagram of a Thermionic Energy Converter (TEC) [11]

The TEC operates in vacuum to minimise electron losses during their transit from the cathode to the anode.

TECs have displayed high power densities ( $20 \text{ W cm}^{-2}$ ) compared to other types of energy devices. The production cost of a TEC per unit energy is also very low. Thermionic devices operate as heat engines, so are limited by the Carnot efficiency. The thermionic cathode is operated at higher temperatures than other energy devices that are limited by the Carnot efficiency, the TEC's efficiency is typically higher. [10]

$$\text{Efficiency} = 1 - \frac{T_{\text{Anode}}}{T_{\text{Cathode}}} \quad \text{Equation 6 [10]}$$

Operating the TEC with a high temperature cathode is more energy-efficient however high temperatures are only reached at a cost so the balance between operating temperature and cost to operate must always be struck particularly if the TEC is being used for commercial electrical power generation. Coupling the heater with the thermionic cathode also presents a challenge as energy will always be lost transferring the energy from the heater to the cathode. Heat energy may be generated by nuclear methods, combustion however solar power does not generate the necessary power per unit area needed to reach thermionic temperatures. Novel concentrated solar power systems address this issue and increase the solar power per unit area by focussing light using parabolic mirrors. [10]

Hatsopoulos proposed a theoretical model of the efficiency of TECs. The flux of electrons through the TEC was calculated using the Richardson equation, modified with exponential terms for each of

the contributors to the potential barrier, and taking into account the work function of the cathode, work function of the anode and the work to overcome the space charge barrier. He calculated that a single device could have an energy efficiency between 10-15% if the setup was optimised with a large temperature difference (722°C) between the anode and cathode and a small separation (0.001 inches) between anode and cathode [7]. The small separation of the anode and cathode serves to improve efficiency by mitigating the effect of negative space charge. Note that the Carnot efficiency for Hatsopoulos' system would be 57%. There are clearly distinct inefficiencies in TECs which are unaccounted for when considering only Carnot efficiency.

The most obvious way to increase the efficiency of the TEC is to reduce the work function of the cathode. Smith points out that improving the properties of the collector can also benefit the efficiency of the system. A NEA collector, Smith argues, at low enough temperatures will provide minimum back-current but will more readily accept electrons leading to a greater TEC efficiency. [12]

The cathode surface must ideally be highly chemically stable over the operational temperature range. A typical cathode material may be susceptible to oxidation at high temperature in its bare form; an inert surface layer which does not inhibit heat transfer may be required.

### **3.2.2 Photo-Enhanced Thermionic Emission (PETE)**

PETE involves using the principles of photoemission and thermionic emission to achieve energy converting devices with higher efficiencies than either of the two technologies individually. The device operates as a solar cell though the high energy photons are thermalized by the material and the thermal energy generated from this process is used to thermally excite electrons to the vacuum level. This technology is deployed in solar cells, typically GaN solar cells, which operate at over 200°C and have combined efficiencies of over 50%. [6] [13]

In conventional photovoltaic cells, which are single pn junctions that are optimised for photon absorption, the quantum efficiency is limited by the Shockley Queisser Limit. This limit is due to the limitations on the energies of photons that can be absorbed by a pn junction with a single finite band gap. Shockley and Queisser also considered the energy spectrum of sunlight and found that the optimum band gap for absorption of sunlight was around 1.1eV which could achieve a maximum theoretical quantum efficiency limit around 30% (Figure 7). [14]

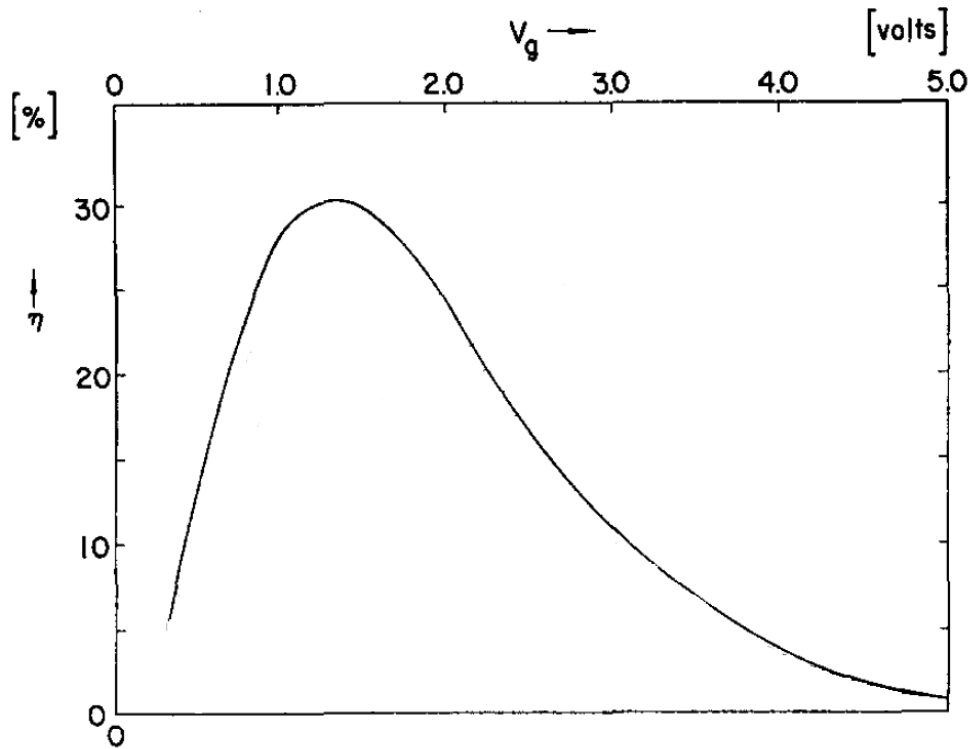


Figure 7 - The Shockley Queisser Limit with efficiency  $\eta$  plotted against band gap,  $V_g$ . The particular plot is for the scenario of minimal radiative recombination ( $f_c=1$ ) [14]

The semi-analytical model used by Varpula based on the thermionic rate equation (see Equation 2) predicted efficiencies of the thermionic devices between 10 and 15% [13]. This is in agreement with Hatsopoulos' model in 1958 [7].

### 3.2.3 Common Thermionic Emitting Devices

Thermionic emitters are an essential component of camera tubes, display tubes, high power radar and broadcast systems [9]. They are also used to generate electrons in electron microscopes and electron beam lithography [15]. A typical GaAs thermionic emitter may emit at  $120 \text{ A cm}^{-2} \text{ K}^{-2}$ . [9]. Tungsten (W) and Lanthium Boride ( $\text{LaB}_6$ ) are good thermionic emitters.  $\text{LaB}_6$  cathodes have high lifetime and capability to produce high emission currents. [15]

Brightness, a measure of the emitted electron density in units  $\text{A cm}^{-2} \text{ sr}$ , is an important factor in many devices. The devices which can emit at highest brightness emit electrons from a small area. The electron emission area of the cathode can be modified by applying a negative potential to areas of the surface where emission is not needed. This is useful in limiting the beam size of the thermionic emitter and it can be done by applying the electric field in a 'triode gun' setup or in a 'limited area cathode gun' setup as in the Imperial College study findings displayed in Figure 8 below. [15]

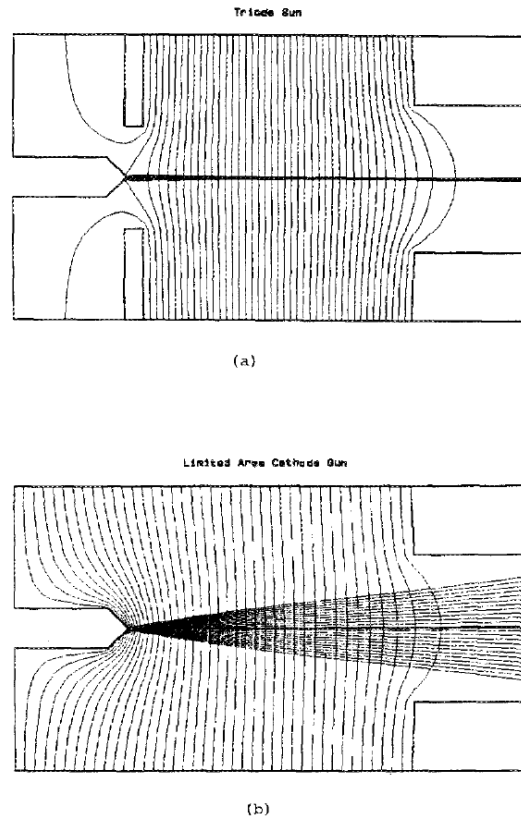


Figure 8 - The computation of equipotentials and trajectories of electrode guns a) Triode Gun b) Limited Area Cathode Gun [15]

### 3.2.4 Diamond as a Thermionic Emitter

Diamond is considered to be a choice for a low temperature thermionic emitter because it is a form of group four element with a stable surface that does not form an oxide layer. The diamond crystal's (1,1,1) face is extremely inert to absorption [16]. This surface can be functionalised with elements that induce a surface dipole to make the diamond surface have a negative electron affinity so that electrons in the conduction band are spontaneously emitted from the conduction band through the vacuum level to the collector.

Diamond is usually an insulator however synthetic CVD diamond doped with boron exhibits semiconducting properties and has a band gap of 5.45eV [17] though the band gap of materials can be modified by adding dopants to the structure.

The thermionic emission capability of diamond at particular temperatures varies greatly depending on the functionalization of the surface discussed in the section 3.2.6.

Producing diamond materials capable of thermionic emission is becoming ever more viable. Through Chemical Vapour Deposition (CVD), poly crystalline diamond can be produced at a rate of  $1 \mu\text{m h}^{-1}$  and with constant improvements made to MicroWave CVD reactors, the deposition rate is ever increasing. [18] [19]

Diamond also has a high thermal conductivity ( $2600 \text{ W m}^{-1} \text{ K}^{-1}$  [17]) which makes for a good thermionic emitter as the diamond can assume relatively uniform temperatures and thus uniform

emission. [20]

Carbon atoms within a diamond lattice form tetrahedral bonds ( $sp^3$ ) to each of the four neighbouring carbon atoms. The lattice can be represented in reciprocal space as in Figure 9.

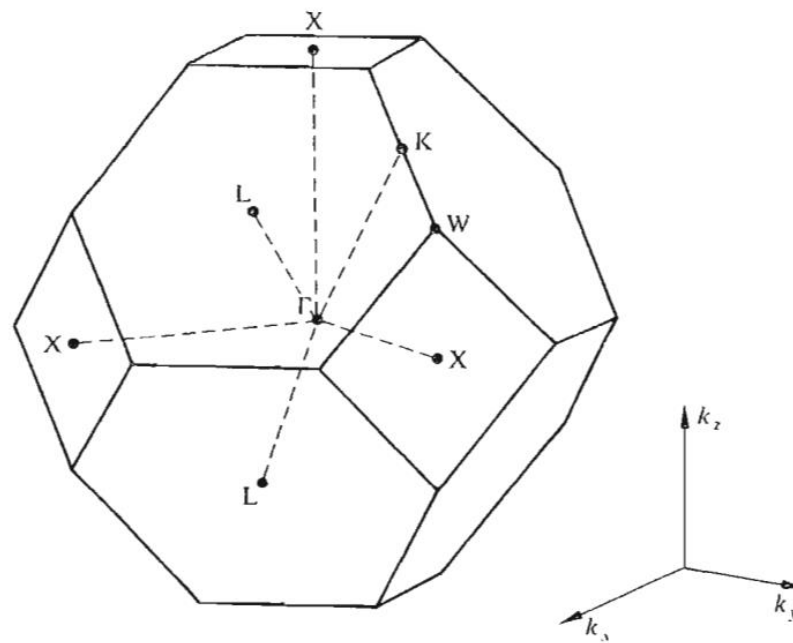


Figure 9 - The reciprocal lattice of a diamond crystal represented in k space with key reciprocal lattice points marked. [9]

Naturally, the carbon atoms at the edge of the diamond lattice are not bonded to four carbon atoms so will have different energies from those atoms which are found in the bulk of the material. See Figure 20 for  $sp_2$  diamond surface structure.

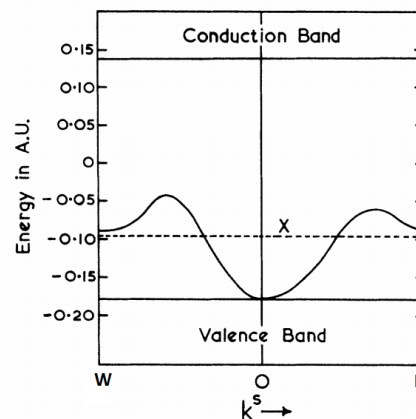


Figure 10 - The band structure of (111) diamond surface states from the centre of the structure to position L and position W on the reciprocal lattice [21]

The band structure of the surface states of the (111) face was calculated in 1964 by Pugh. [21]

### 3.2.5 Doping of Diamond

The energy levels of the Boron acceptor level and the P and N donor levels are shown:

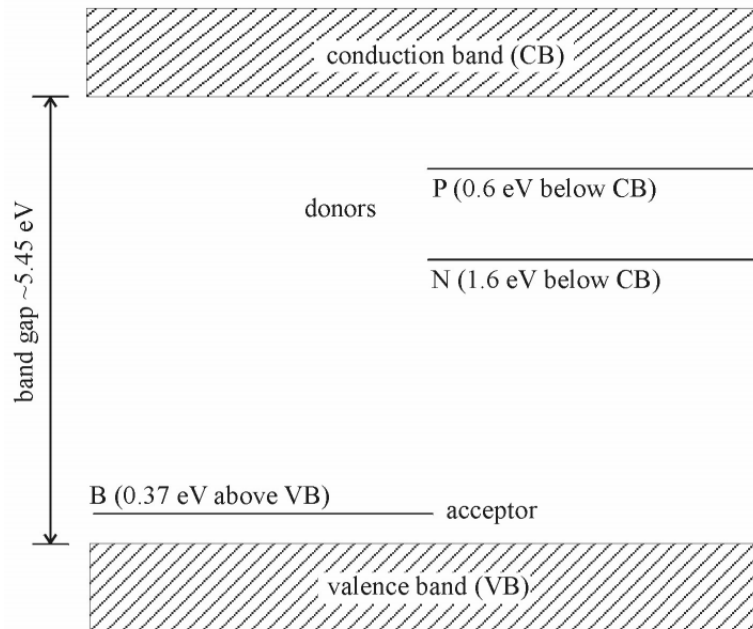


Figure 11 - Energy levels of diamond with common dopants [17]

The addition of boron to the diamond structure creates an energy level close to the valence band which to which electrons from the valence band may be promoted. The holes donated by the boron atoms increase the electron mobility in the valence band because the valence electrons have more unoccupied energy levels which they can move in to. Due to the number of possible configurations of the system,  $W$ , increasing, the entropy,  $S$ , also increases.

$$S = k_B \ln(W) \quad \text{Equation 7}$$

Boron can be easily incorporated in the CVD diamond [22] to make boron-doped diamond (BDD). It can be added during the manufacture process as diborane gas, diffused or implanted at high temperatures (1450°C). Papers indicate typical boron dopant concentration would in the range of  $5 \times 10^{20} \text{ cm}^{-3}$  [22] and  $4 \times 10^{19} \text{ cm}^{-3}$  [23].

Boron doping causes electronic transitions within the lattice where the energy of transition is equal to that of a photon in the infra-red region. The Raman spectrum peaks at  $2450 \text{ cm}^{-1}$  and  $2820 \text{ cm}^{-1}$  indicating presence of Boron [24] [25]. The Raman peak for crystalline diamond falls at  $1332 \text{ cm}^{-1}$  [23].

n-type CVD diamond has been produced most commonly with phosphorous or nitrogen. N-type donors act as electron donors so increase the electron density within the lattice however n-type doping of diamond usually results in a high defect density in the diamond structure which as discussed in 3.2, gives a reduced minority carrier lifetime and consequently reduces thermionic emission. n-type doping with nitrogen also results in a compact lattice leading to low solubility for other species. N-type doping with P or N leads to deep energy levels which are of no use for room temperature semi-conduction. [22]

Diamond has been successfully doped with phosphorous using microwave CVD. Koeck measured the P-doped diamond to have an extremely low work function at 0.9eV when hydrogen terminated (H-terminated). [26]

Nitrogen doped (NDD) has been produced by Koeck with samples producing very low work functions of between 1.5eV and 1.9eV measured using UPS. The H-terminated NDD emitted thermions at temperatures less than 400°C [23]. Thermionic emission was measured under UHV conditions ( $10^{-10}$  Torr) and samples were taken up temperatures of 1200°C. Emission current peaked at  $1.2 \text{ mA cm}^{-2}$ . [23]

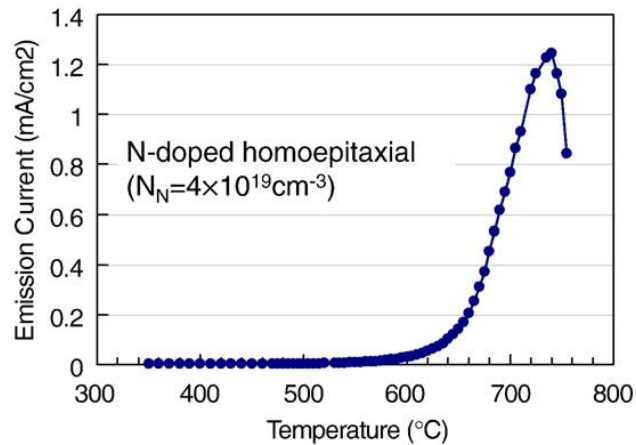


Figure 12 - Emission characteristics of N-doped diamond. The emission begins around 600°C and decreases sharply at 740°C due to desorption of the hydrogen termination. [23]

Nitrogen doped diamond has been produced in a study by Koeck with hydrogen and titanium monolayer surfaces for NEA [27].

By fitting the Richardson equation to experimentally emission data, the Richardson constant,  $A$ , of the NDD can be shown to be dependent on the work function.  $A$  was calculated to be  $0.1 \text{ A cm}^{-2} \text{ K}^2$  at a work function of 1.5eV and  $10 \text{ A cm}^{-2} \text{ K}^2$  at a work function of 1.8eV [8].

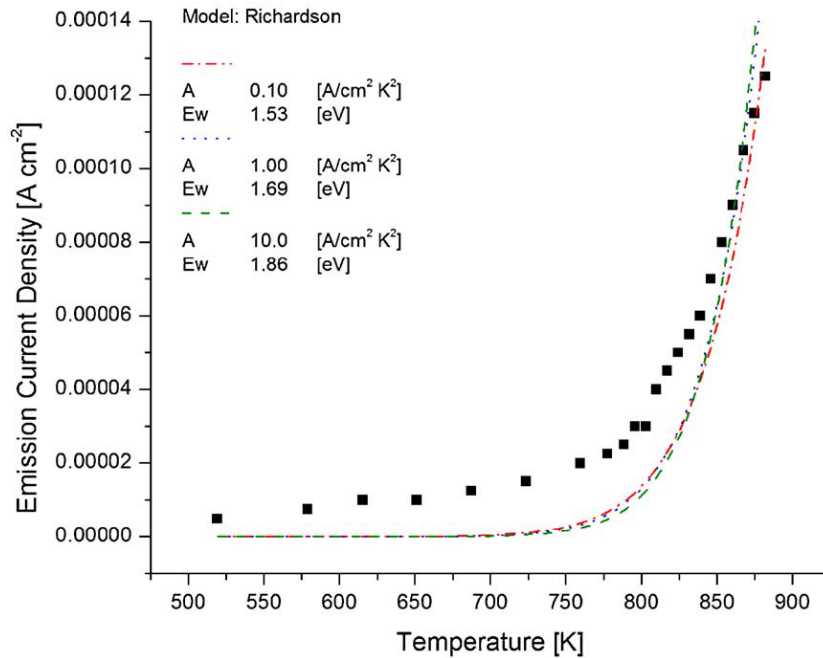


Figure 13 - Emission current density plotted against temperature in order to model experimental data from NDD against the Richardson Equation Curves. [8]

Advances in developing an n-doped semiconducting CVD diamond are often made using computational physics to find dopants that will produce shallow energy levels. No computational method is perfect in predicting the behaviour of a dopant. One computational method is density functional theory (DFT) which predicts the energetics of a dopant from its ground energy using periodic boundary conditions to model an infinite lattice. Li has been suggested by Goss as a suitable element to provide shallow donor levels for good conduction in diamond [22].

Othman suggests that the Li may be electrically inactive in the Li-doped material because the lithium is able to diffuse across grain boundaries and form electrically inactive clusters [28]

Othman performed experiments to incorporate both N and Li into the diamond lattice simultaneously. Lithium acts as an interstitial donor. Nitrogen was added through the inclusion of ammonia during the hot filament (HF) CVD growth phase. Li was subsequently added through melting Li<sub>3</sub>N crystals onto the diamond surface and allowing diffusion at 800°C. Secondary Ion Mass Spectroscopy (SIMS) was used to confirm the successful incorporation of these elements into the lattice with an estimated depth of 100-200nm. [29]

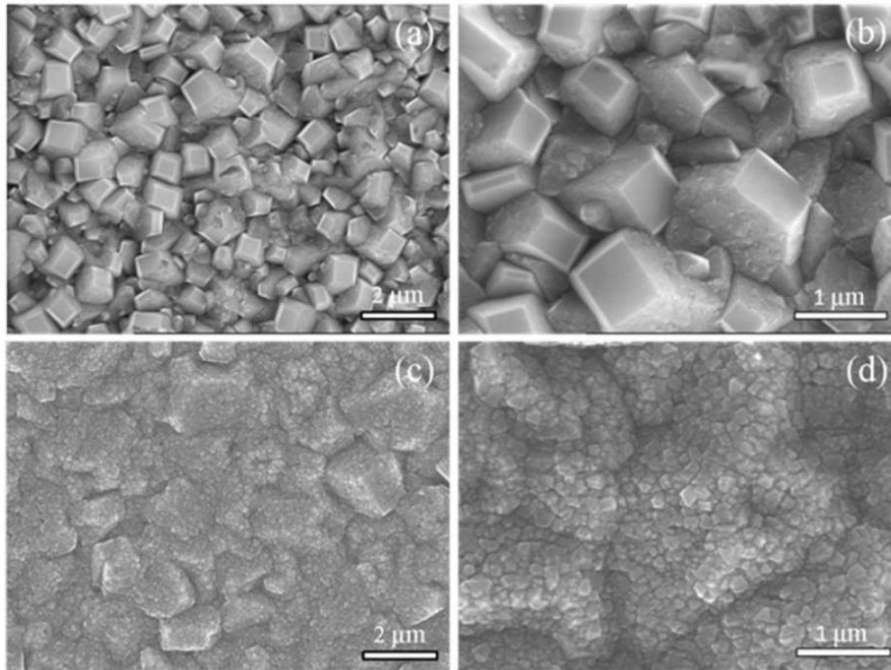


Figure 14 - (a) and (b) N- doped diamond SEM showing crystal facets. (c) and (d) N-Li-doped diamond showing roughened crystal facets. [29]

The lithium concentration was  $1 \times 10^{21} \text{ cm}^{-3}$ . The nitrogen to lithium ratio was 9:1 in order to use the nitrogen atoms as traps to immobilise the lithium in the lattice. Despite the attempt to immobilise the Li atoms to allow them to be electrically active, the resistivity of the material was still high at 15-50M $\Omega$ .- this is a slight drop from the usual range of 10-20M $\Omega$  for room temperature NDD however the poor electrical activity is suspected to be due to the Li and N diffusing into grain boundaries. [28].

### 3.2.6 Modifying the diamond surface for NEA

Diamond can be given a NEA surface by chemisorbing a highly polar species to the diamond surface. A common surface termination which provides an NEA surface on diamond is hydrogen [30] though lithium oxide, lithium [20], titanium [27] and caesium oxide [31] have shown NEA results as well.

The presence of a NEA surface can be tested for by exciting electrons into the conduction band and measuring the energies of the emission. Measurement methods include Photo Emission Electron Microscopy (PEEM) which uses a UV lamp to excite electrons and Field Emission Electron Microscopy (FEEM) which uses an electric field to excite electrons [27].

In a study carried out at Michigan State University, the lowest observed work function achieved by the H-termination of BDD was 3.95eV and the lowest work function achieved by the nitrophenyl terminated diamond was 3.88eV [32]. The work functions of the diamond surfaces were measured using Thermionic Electron Energy Distribution methods. The stability of the hydrogen surface was shown to be low when the sample was heated past 725°C to a maximum of 1085°C [32]. Other sources indicate lower temperatures for the beginning of the H desorption process. Koeck states that hydrogen desorption was observed at 725°C [27].

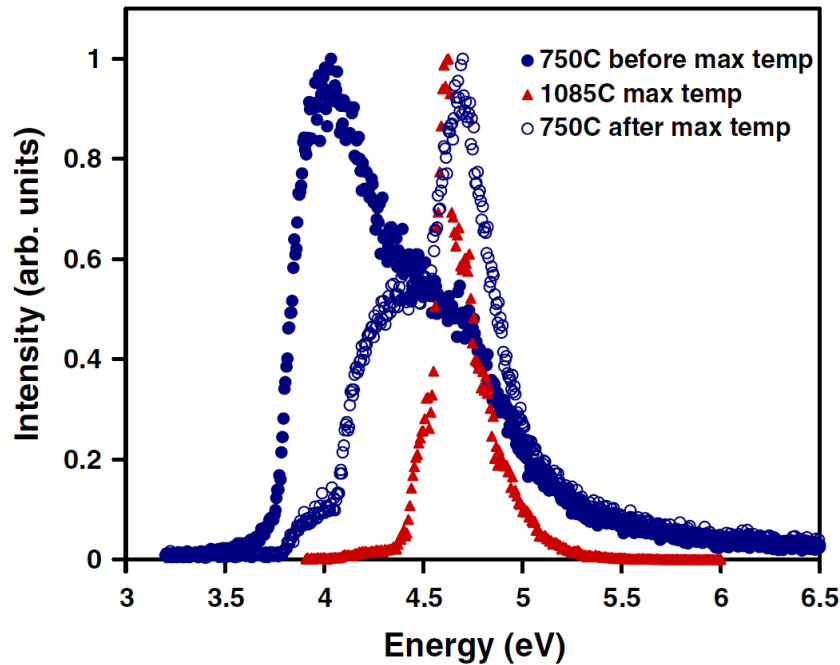


Figure 15 - The electron energy distribution for a H-terminated diamond sample showing an increase in the areas of high work function when exposed to temperatures beyond 750°C. [30]

It was found that the after H desorption, the surface could be re-terminated with H successfully.

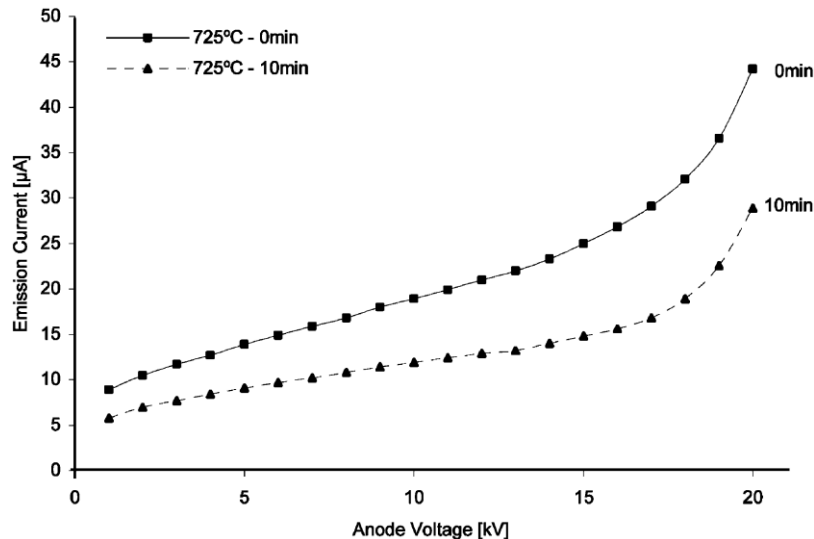


Figure 16 - The emission current of H terminated nitrogen doped diamond at 725°C decreases over time demonstrating the instability of the H-termination past 725°C. Cathode- anode separation is 4mm. [27]

Hamza in a separate paper also studied desorption of hydrogen from the BDD surface and concluded that hydrogen was being lost from near surface states in the diamond lattice as well as from the surface layer. Ultraviolet Photoelectron Spectroscopy (UPS) was used to determine the structure of the hydrogen on the diamond surface and it was found that carbon atoms at the surface form dimers with a monohydride termination (see Figure 20) [33]. Using copious amounts of hydrogen during termination will result in a polyhydride surface [31].

In another study by Koeck, the hydrogen terminated BDD was tested at various temperature ranges and its emission was found to start at 500°C and peak at 720°C. The sample emitted up to 45µA at 725°C [27] (see Figure 16 - The emission current of H terminated nitrogen doped diamond at 725°C decreases over time demonstrating the instability of the H-termination past 725°C. Cathode- anode separation is 4mm. Figure 16). In the same study, Ti terminated BDD was tested and the Ti surface exhibited emission from 700°C up to 950°C and reached emission currents of over 90 µA (see Figure 17) [27]

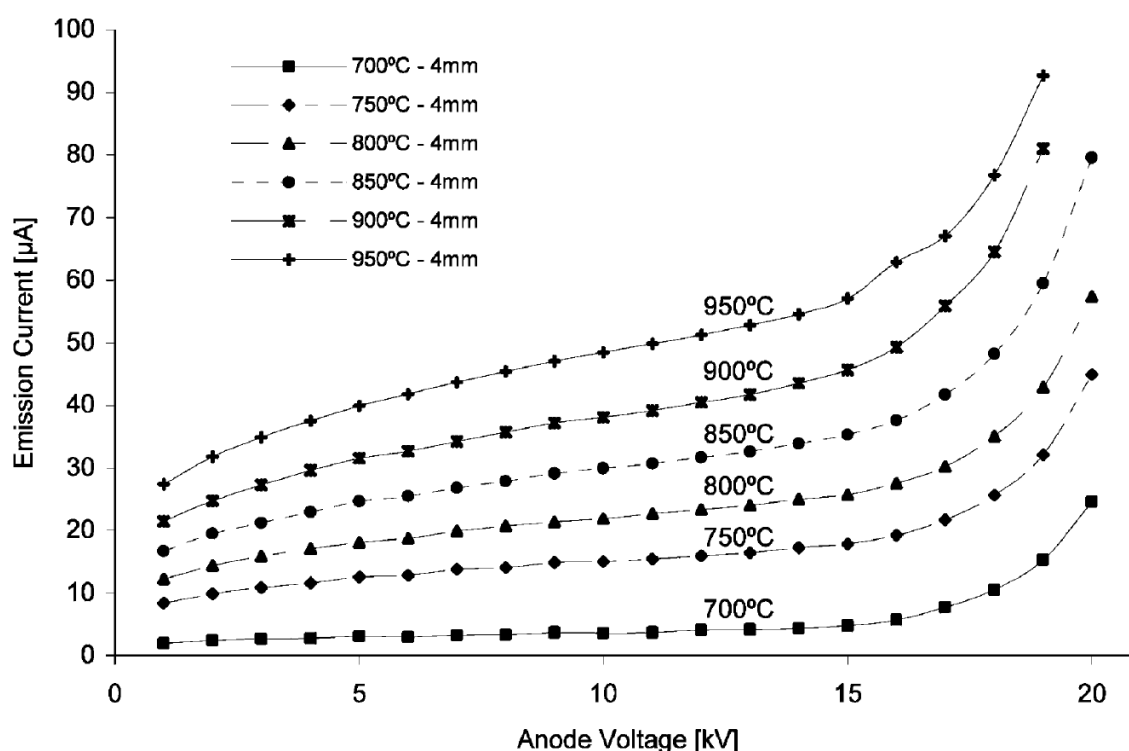


Figure 17 - The emission current of Ti-terminated diamond at temperatures between 700°C and 950°C with cathode-anode separation of 4mm. [27]

A Cs-O monolayer can reduce the work function of the BDD surface to 1.25 eV [20] [31]. The effectiveness of the CsO termination and the bonding of the CsO with the carbon surface depends entirely on the preparation method. The Cs-O termination which was hydrogenated at 300K (P3) expressed instability when exposed to oxygen. The sample only exhibited a NEA peak in the UPS at temperatures less than 450K. The other caesium oxide terminated sample, P1, which was acid etched then annealed at 1400K and P2 which was oxygenated at 300K displayed stability when exposed to oxygen and thermal stability of its NEA properties up to 660K. [31]

Summary of the salient spectroscopic features of P1, P2 and P3

Pretreatment methods	NEA peak:Cs 5p <sub>1,2</sub> intensity ratio	XPS core-level shifts after caesiation (eV)	Threshold temperature for complete attenuation of NEA after air exposure (K)	Stability of NEA to O <sub>2</sub> /air exposure
P1: ex situ acid etching and vacuum annealing to 1400 K	~2.8	1.2	670	stable
P2: oxygenated at 300 K	~2.2	1	650	stable
P3: hydrogenated at 300 K	~1.2	0.3	450	unstable

Table 1 - The spectroscopic features of CsO terminated diamond samples P1, P2 and P3. [31]

Using X-ray Photoelectron Spectroscopy (XPS), the structure of the Cs-O prepared samples, P1, P2 and P3 were analysed. The XPS showed that P1 exhibited a Cs-C bond at the diamond surface, P2 exhibited a Cs-O-C bond and P3 exhibited a Cs-CH<sub>x</sub>-C structure which accounts for their different behaviours and NEA values. Loh explains in the paper that the proximity of the Cs charge is key to enhancing the NEA effect through band bending (the bending of the conduction band down closer to the vacuum level) and that in P1 the structure allows for the most band bending, followed closely by P2 and a long way ahead of P3 which has the CH<sub>x</sub> group which is able to dissipate charge density and lessen the effect of the band bending at the diamond surface. [31]

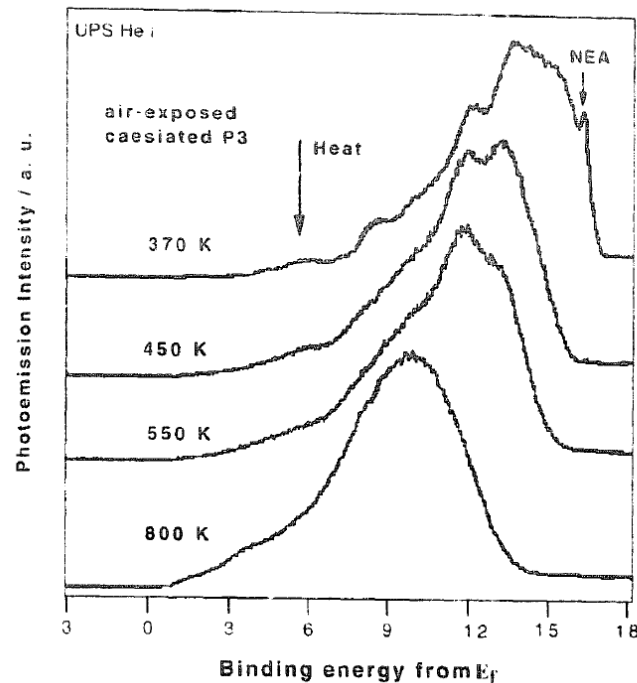


Figure 18 - The Ultraviolet Photoelectron Spectrum of the air exposed CsO termination at various temperatures. The sample, P3 was hydrogenated at 300K during preparation and had an unstable termination which did not express an NEA peak past 450K. [31]

The nitrophenyl termination on BDD showed signs of degrading past 750°C and no emission data was published in Koeck's paper. [27]

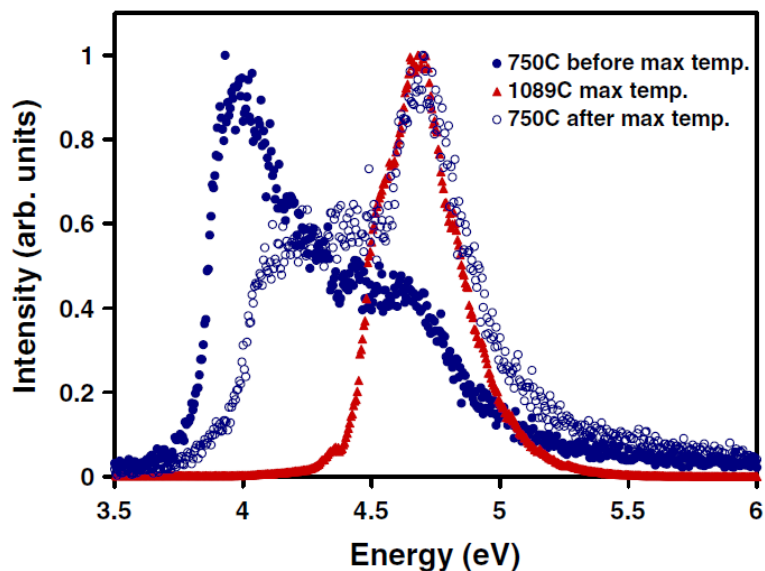


Figure 19 - Electron energy distribution of nitrophenyl terminated BDD. After heating to 1089°C, even when returned to 750°C the work function has remained higher across a greater proportion of the surface area. [32]

### 3.2.7 Li, LiO terminations and computational analysis of diamond surface structure

The LiO surface termination shows high stability and low work functions which makes it a viable alternative to Cs on BDD structures [20] [11]. In Thomas Martin's PhD thesis ([11]), the interaction of Li with the diamond C(100) and C(111) face was analysed using DFT with and without the presence of oxygen. When Li was modelled adsorbing to the bare C(100) face, the surface exhibited an electron affinity of -1.07eV to 2.7eV though the Li surface was unstable. The Li surface upon an oxygenated diamond surface exhibited lower calculated electron affinity with a minimum at -3.97eV and had much stronger adsorption to the surface with an adsorption energy as high 4.7eV. The DFT computationally calculated work function of the diamond changed by -3.9eV down to a value of 1.6eV [20] [11].

Low energy electron diffraction (LEED) and UPS were carried out to image the structure of an experimentally prepared sample. On the Li-O-C sample, the surface termination had remained but the unstable Li-H-C termination showed no trace of Li shortly after the sample preparation. UPS results gave a work function for the LiO of  $2.8 \pm 0.1\text{eV}$  and a NEA of  $-2.1 \pm 0.1\text{eV}$ . The LiO surface was stable up until 1218°C. [11]

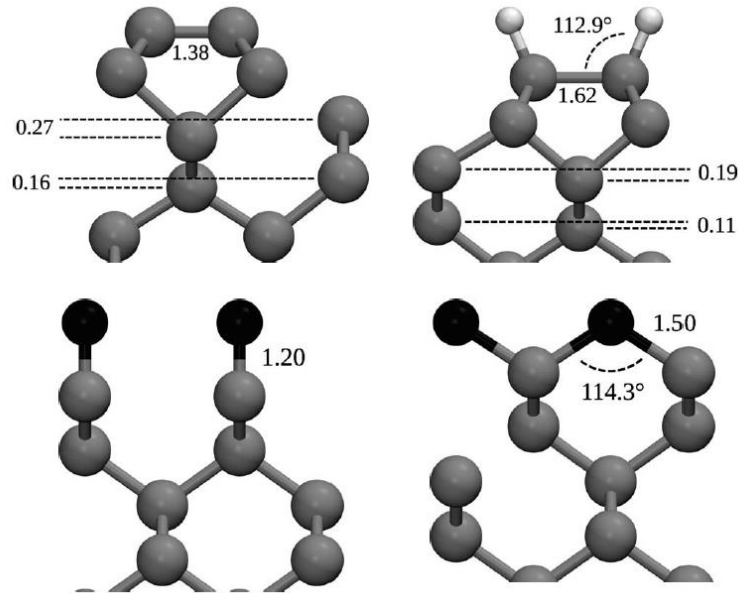


Figure 20 - The optimized structure for a) Bare diamond surface edge (C100) b) H terminated-diamond surface c) Carbonyl-terminated diamond d) Ether-terminated diamond [20]

The lithium-terminated diamond structure depends on the number of Li monolayers (ML) on the surface. Figure 21 shows the structure of the Li-Diamond surface at 0.5 ML and 1 ML. Li has a significant lower binding energy when  $ML > 1$ . [20]

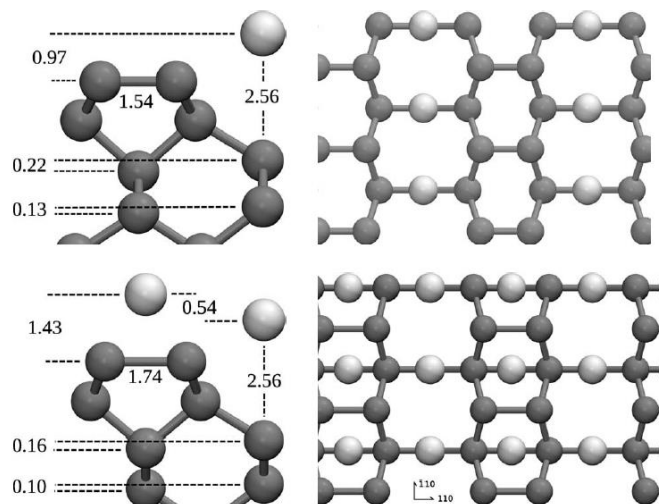


Figure 21 - The lithium ion occupies interstitial sites at the diamond surface in its lowest energy states. Top is the structure for 0.5ML Li and bottom is the structure for 1 ML Li adsorption on C(100)-(2x1) [20]

In a study at Bristol University by Andrade in 2014,, the work function of boron doped, lithium oxide terminated material was measured using Kelvin Probe Force Microscopy (KPFM), a form of non-contact Atomic Force Microscopy (AFM) which measures the contact potential difference (CPD) between the tip of the cantilever and the material surface – effectively the work function. KPFM can be used in two modes, Amplitude Modulation (AM-KPFM) which detects the electrostatic force on the material surface and Frequency Modulation (FM-KPFM) which is sensitive to the gradient of the electrostatic force. The measurements were carried out under Ultra High Vacuum (UHV) and the

work function showed a range of work functions between 4.31eV and 4.7eV with a median of 4.52eV. The work function across the diamond surface was shown to vary substantially and that even neighbouring polycrystalline facets could have a variation in work function of up to 400meV. Work function measurements were also carried out on an identically prepared sample by Photo Emission Electron Microscopy (PEEM) which measures secondary electron emission energies to calculate work function data. The benefits of PEEM are the high lateral resolution of 150nm and sensitivity to work function changes of approximately 20 meV. The work function measured by PEEM was between 3.9eV and 4.4eV with a median of 4.05eV. The work function measurements were then related to the topology of the diamond surface.[34]

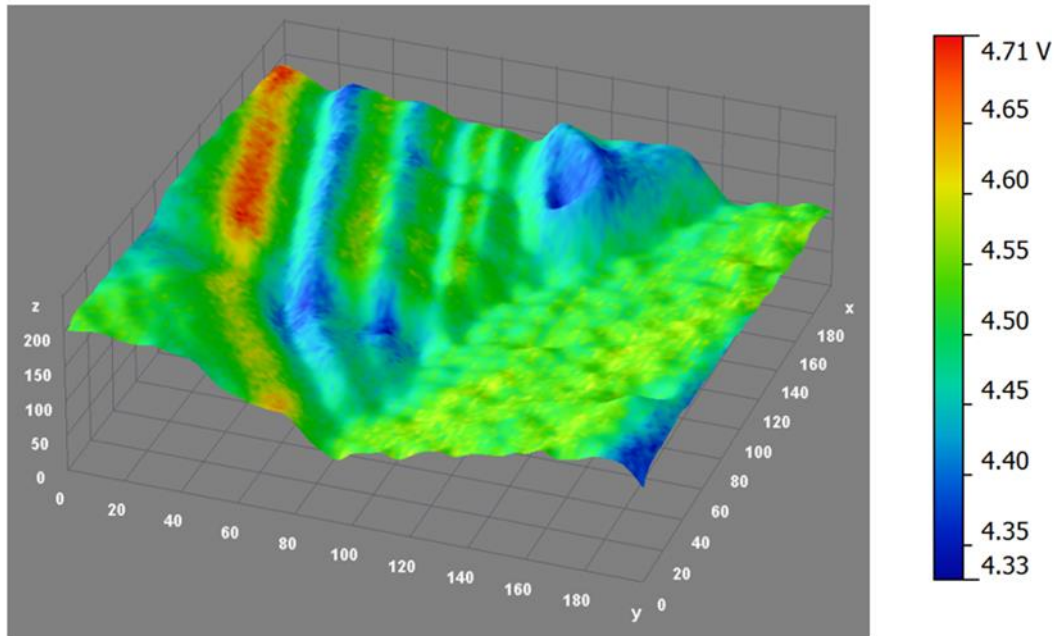


Figure 22 - Distribution of work functions measured using PEEM across boron-doped lithium oxide terminated diamond surface superimposed upon the topology of the surface. [34]

### 3.3 Radiation conversion and transport in diamond. Role of bulk and surface defects.

Undoped polycrystalline diamond is an insulator. [35] Defects in the bulk of the diamond lattice provide acceptor energy levels which electrons may occupy. The electron mobility in diamond is enhanced by these 'traps'. Transport in diamond is approximately all attributable to one type of carrier - holes. Electrons contribute only 5% to the collected charge. The diamond conductivity can therefore be approximated to be proportional to the hole concentration. [35]

Surface defects with large surface charge bend the bands of diamond and provide NEA. Surface defects can also act as traps so can cause electron-hole recombination centres.

Polycrystalline diamond has grain boundaries (amorphous graphite regions) which act as traps [36]. The grain boundary energies act at acceptor states approximately 1eV above the valence band of the material. [35]

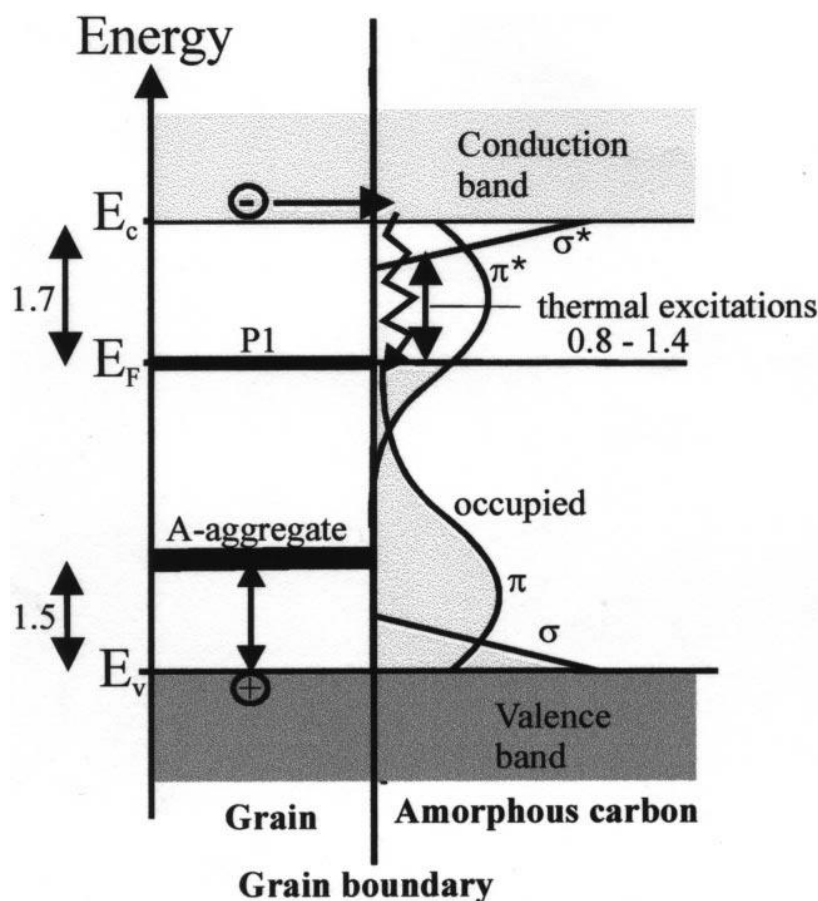


Figure 23 - Band structure of amorphous carbon and the grain at the grain boundary demonstrating the trapping of electrons in antibonding states.  $E_F$  denotes the Fermi energy. A-aggregate denotes the acceptor aggregate. All energies are in units of eV. [36]

The additional energy levels available to electrons in the amorphous carbon/ graphitic region at the grain boundaries allow conduction through the polycrystalline diamond lattice that would not be possible in single crystal diamond [37]. UV light can be used to increase the conductivity of polycrystalline diamond [38].

Extrinsic defects, as discussed in 3.2.5, also act as traps. The benefit of using extrinsic defect traps is that the concentrations of the defects can be adjusted for varying conductivity. With enough doping, the bands of the material can overlap to the extent that it will have metallic conductivity. The choice of dopant affects the energy of the acceptor/donor level which is introduced. For increased conductivity it is most useful to have dopants which provide acceptor levels which are close to the energy of the valence band (shallow doping). Shallow dopant energy levels make low temperature thermionic devices far more viable [26].

Interestingly, heavily boron-doped diamond ( $10^{21}$  B atoms  $\text{cm}^{-3}$ ) results in superconducting behaviour below 4K though the superconductor expulsion of magnetic field is not homogenous due to the non-uniform distribution of B atoms in the lattice [39]. The (111) BDD films have greater boron pair densities than the (100) BDD films of equivalent dopant concentration and thus have a higher critical temperature at which they transition to superconductive properties [40].

### 3.4 Absorption, Plasmons and Heat Transport

#### Absorption

In laser heated thermionic emission, it is preferable to reach the highest temperature that the setup can facilitate. An understanding of how energy is transferred from the CO<sub>2</sub> laser as infrared radiation to the thermionic diamond cathode as heat must be attained.

University of Reading studies [41] show that infrared radiation acts upon an infrared optically active material to induce heat. An infrared optically active material is a material which undergoes electron excitations upon the incidence of infrared region light. The energy of the light corresponds to the energy gap between the two electron energy states. The electromagnetic radiation produces an oscillating dipole moment which transfers energy to the lattice in the form of a phonon. The phonon is a lattice vibration which results in radiation to heat energy transfer. The susceptibility of the lattice to induced phonon processes depends on the lattice constant of the structure. [41]

A study into the BDD absorbance of infrared radiation was carried out by Gheeraert et al. The transition from the ground state to the first excited state of the bound hole is infrared optically active. The study showed that the absorption co-efficient,  $\alpha$ , was linearly related to the concentration of boron in the diamond lattice. High boron dopant concentrations ( $2 \times 10^{19} \text{ cm}^{-3}$ ) saw absorption coefficients up to  $170 \text{ cm}^{-1}$ . [42]

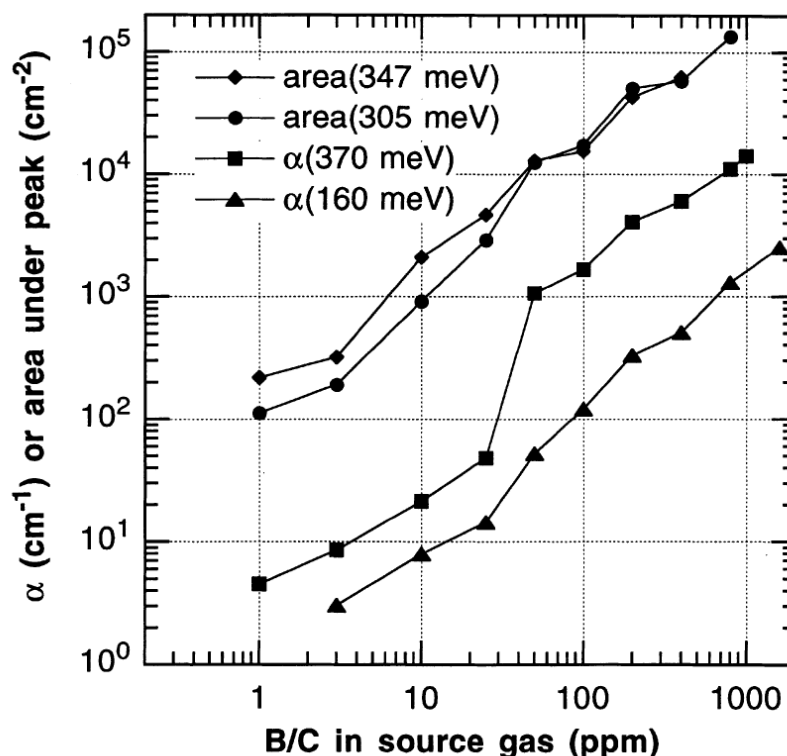


Figure 24 - The relationship between absorption co-efficient absorption coefficients and boron dopant concentration for single phonon absorptions (160meV) and photoionisation (370meV). [42]

### Heat Transport in Diamond

In similar fashion to the conductivity of diamond, the grain boundaries of polycrystalline diamond greatly affect the heat transport in the structure. The diamond-graphene interface at the grain boundary involves a change in lattice constant which causes a mismatch in the lattice vibrational spectra and inefficiency in phonon transport across this region known as Kapitza resistance. [43]

$$R_K = \frac{Area \times \Delta T}{Q} \quad \text{Equation 8 [43] [44]}$$

$R_K$  is the Kapitza resistance in  $m^2 K W^{-1}$ ,  $\Delta T$  is the difference in temperatures of the two lattices and  $Q$  is the heat flow across the area.

Strivastava describes the effect of Kapitza resistance in the acoustic mismatch model (AMM) with a transmission co-efficient,  $\tau_{r1 \rightarrow r2}$ , which represents the probability of transition for the phonon (plane wave) to cross the interface. The transmission co-efficient is defined by the acoustic impedances,  $Z_i$ , of the materials. [45]

$$\tau_{r1 \rightarrow r2} = \frac{4Z_1 Z_2}{(Z_1 + Z_2)^2} \quad \text{Equation 9 [45]}$$

Loh studied thermal transport in diamond and found the AMM model to be inconsistent to experimental results by an order of magnitude. Loh attributes the discrepancies to the failure of the model to account for more complex effects such as elastic phonon scattering at the interface, inelastic scattering, electron-phonon resistances, interface roughness and the effect of thermal flux. Using a model that better accounts for thermal flux, Loh simulated the diamond-graphene interfaces computationally and found significant reduction in phonon conductivity at interfaces close to lattice vacancies. The distance of the vacancy to the interface affected the relative phonon velocity in the two materials and thus affected thermal transport. [46]

A computational study into solid-solid superlattice thermal transfer found that the fewer the layers in a system, the higher the efficiency of heat transfer. [47]

### Plasmons

Laser-heated thermionic cathodes may be coupled to metal absorbers designed to absorb the laser energy efficiently. Considering the absorption mechanics of at the metal surface will ensure maximum absorption.

Localised surface plasmons are collective oscillations of conduction electrons in metal particles. Incident light on a metal surface produces an oscillating dipole moment which creates surface plasmons and leads to polarization charge on the surface of the metal. Polarization acts as a restoring force, making the plasmons oscillate at the surface plasmon resonance frequency [48].

Plasmon effects can be used as a method of increasing the absorption of light as the energy is transferred more efficiently at the surface plasmon resonance frequency. The wavefunction of the plasmon can be confined by fashioning the metal surface into a grating of similar wavelength to that of the incident light. The grating-plasmon interaction creates a higher probability of absorption of light. [49]

### 3.5 A note on the manufacture of CVD Diamond

Diamond films may be grown by hot filament chemical vapour deposition (HF CVD) which involves injecting methane gas at high pressures (20-30 Torr) into a vacuum chamber contained a hot tungsten filament. The filament is typically made from tungsten or tantalum as these metals can withstand the operational temperatures of between 700 and 900°C. A silicon or molybdenum substrate is usually used as a growth platform for diamond (heteroepitaxy). The methane forms diamond upon nucleation points on the substrate [18].

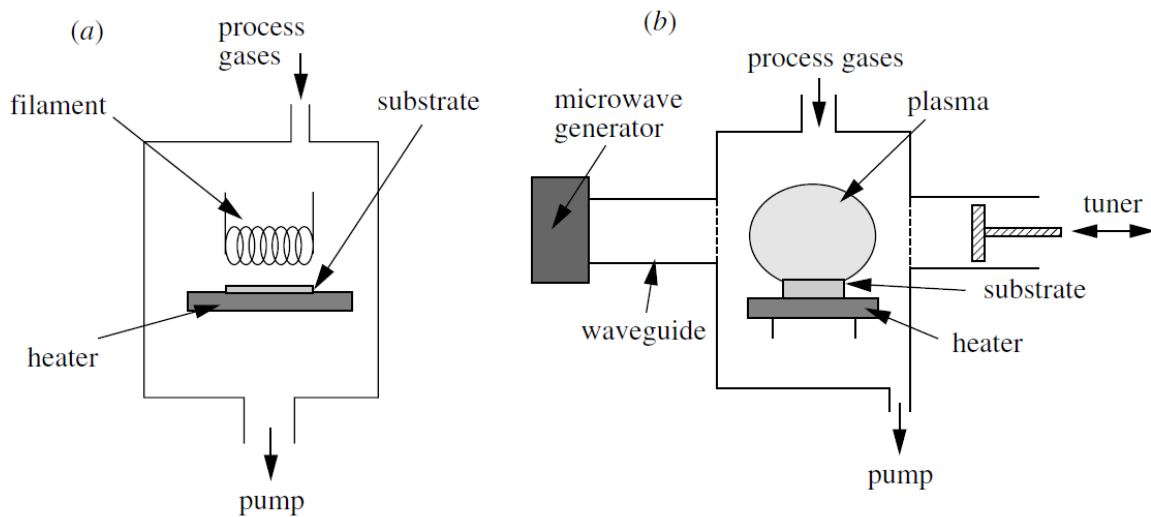


Figure 25 -Schematic diagrams of HFCVD and MWCVD reactors for diamond growth [18]

The temperature range which CVD diamond can be grown in is from ~ 600°C to ~1200°C. Beyond this range, other forms of carbon such as graphite and amorphous carbon may be formed. The phase behaviour of diamond is expressed in Figure 26.

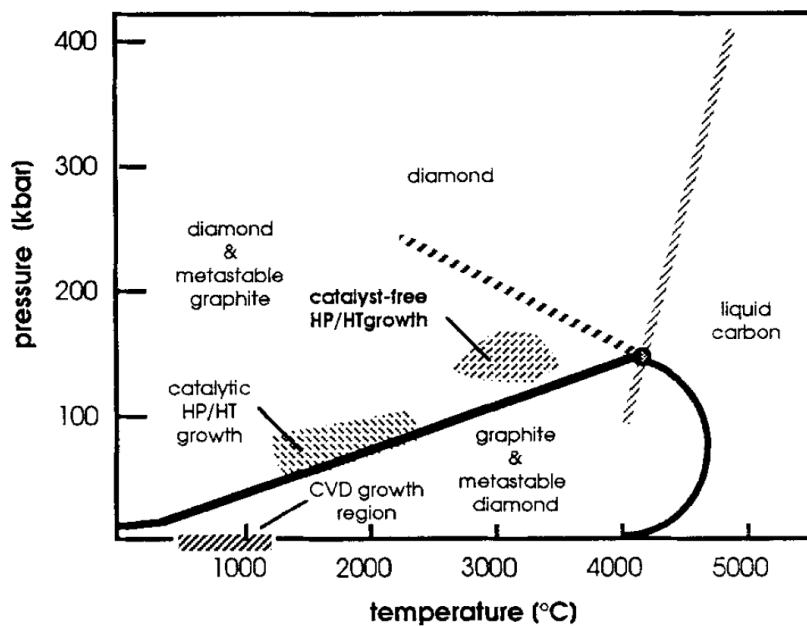


Figure 26 - The phase diagram for the growth of diamond [50]



### 3.6 Diamond potential for Photo-Enhanced Thermionic Emission (PETE)

The (1,1,1) surface of diamond photo-emits when exposed to light of energy greater than the photothreshold ( $\phi_{th} = 5.5 \pm 0.05 \text{eV}$  [16]) as well as thermionic emission. Thermionic energy converter's overall efficiency can be improved by utilising photoemission for additional current generation [6]. The challenge with diamond is achieving good photoemission because the band gap of diamond is so large.

Boron-doped diamond exhibits high quantum efficiency of between 40% and 70% when illuminated with visible and near UV wavelength light [16]. UV light can be used to increase the conductivity of polycrystalline diamond [38]

Koeck leads the field again in a study on diamond PETE devices using NDD at temperatures up to 340°C. Koeck uses 1.5eV work function NDD and shows that additional current is emitted when the sample is illuminated with light with wavelength 340-550nm. The sample begins thermionic emission at a temperature of 220°C which is extremely low and may even be viable for commercial use in solar cells. Less-optimistically, the photoemission begins to decrease at 220°C, due to phonon scattering in the lattice. Lattice scattering can be modelled as a probabilistic event where the probability (Poisson's term) depends on the temperature of the material [51].

## 4 Experimental

The object of the experimental work was to optimize the Bristol University laser heated thermionic emission setup and use it to study the parameters which affect thermionic emission from diamond.

### 4.1.1 Initial Setup

The available equipment for the laser heated thermionic setup in the diamond lab is:

- 40W CO<sub>2</sub> laser with wavelength 10.2-10.8µm (Average 10.6 µm) for generating infra-red radiation to laser-heat the thermionic cathode.
- Vacuum chamber operating at pressures between  $9.6 \times 10^{-6}$  –  $1.2 \times 10^{-7}$  Torr. All heating tests and thermionic tests were performed under vacuum conditions.
- Nd-YAG laser cutter (532nm) used for all milling/cutting operation.

### 4.1.2 Samples Used

*Chemical Vapour Deposition/production method*

All samples were 1cmx1cm by a depth of 0.3mm in order to fit in the thermionic setup.

Sample	Material(s)	Production
A	BDD (H-terminated, Li Diffused)	BDD grown in HFCVD with H <sub>2</sub> , CH <sub>4</sub> and NH <sub>3</sub> gas injection. H-terminated using microwave induced plasma at 550°C for 10 minutes. Slowly cooled in hydrogen atmosphere. Li <sub>3</sub> N crystals are diffused

		into surface.
B	Molybdenum (Bare)	Cut in the Nd-YAG laser cutter. Unaltered Mo surface.
C	Molybdenum with grating	Cut in the Nd-YAG laser cutter. Surface altered for increased absorption. See 4.2.2.
D	Molybdenum with 2 micron grown BDD film	Mo was cut in the Nd-YAG laser cutter. A BDD film was grown to 2 $\mu$ m using the HFCVD reactor.
E	BDD + Molybdenum with 2 micron grown BDD film.	Sample A was sandwiched with Sample with sample D on the absorbing side of the cathode.
F	BDD (H-terminated)	Sample A with previous H-termination desorbed off at 720°C. Sample is reterminated with hydrogen using MW induced plasma at 550°C for 10 minutes and then slowly cooled in a hydrogen atmosphere. No lithium diffusion is performed.

Table 2 - Properties and manufacture of samples A to F

## 4.2 Optimising the Thermionic Emission Set-up

### 4.2.1 Mounting the diamond sample

The diamond sample mount was designed so that the sample would have point contacts with the diamond for minimal thermal transmission. Molybdenum was the chosen material for the mount because it was readily available and had similar thermal expansion to diamond. The mount had prongs fashioned to allow flexibility in the structure to account for the thermal expansion of diamond. The molybdenum mount was designed using CAD and cut in the laser cutter for accurate cutting to ensure that the holder would hold exactly 1cm x 1cm diamond pieces.

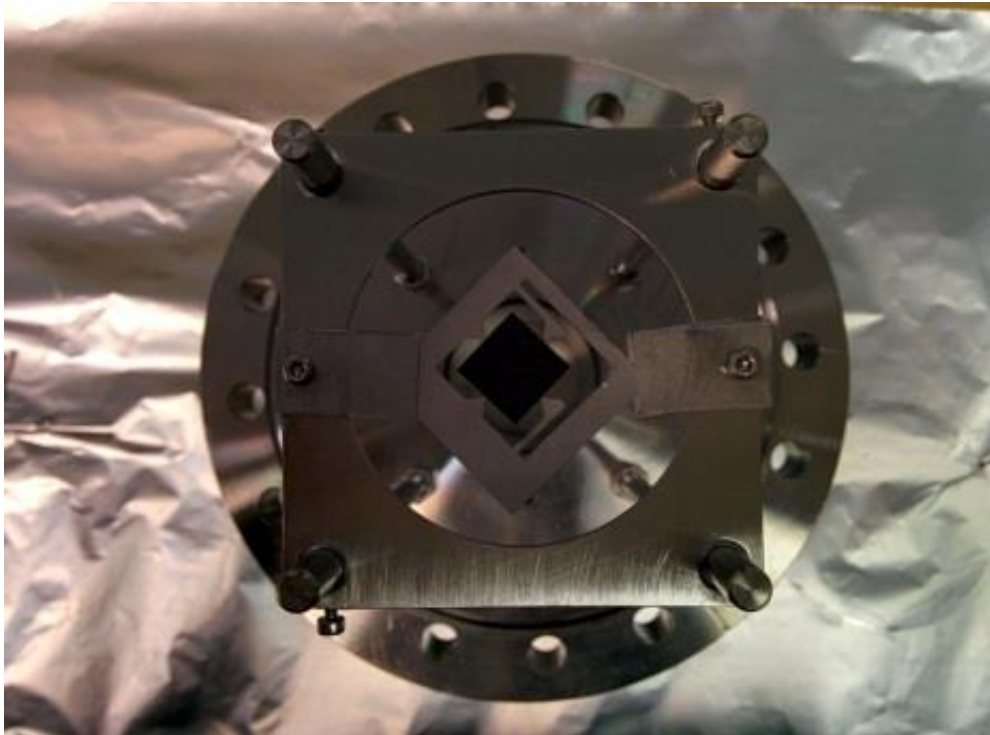


Figure 28 - a 1x1 cm diamond sample (black square) being suspended in a molybdenum mount.

The molybdenum mount was clamped to the spurs of the vacuum chamber unit so that the diamond sample could be precisely lined up with the focus of the laser. The mount was also positioned so that the diamond piece could be as close as possible to the anode for thermionic emission tests.

#### 4.2.2 Enhancing the Absorption of the Molybdenum Plate

The reflectivity of molybdenum is around 95%. The absorption of the Molybdenum plate was increased by creating periodic trenches in the surface of the Molybdenum plate of the order of the wavelength of the CO<sub>2</sub> laser (10 microns) to induce surface plasmons (see 3.4) based on the advice of Bristol Universities Photonics group. A surface with trenches of the periodicity of the wavelength of the CO<sub>2</sub> laser is optimal for inducing surface plasmons and maximising infrared radiation conversion to heat.

The optimal periodic trenches were 6 $\mu$ m wide with 4 $\mu$ m between each trench. The trenches were cut with the diamond group laser cutter.



Figure 29 - Optimal Mo plate for absorbing CO<sub>2</sub> laser beam.

The 6 micron width of the trenches is very similar to the beam width of the laser cutter which made it difficult to get the clearest cut trenches. When viewed in the Scanning Electron Microscope, the

trenches tended to have uneven depth and have a curved profile rather than a square cut profile. The material which had been pulse-lasered from the trench had not been evaporated and instead formed a Mo lip at the side of each trench. Trenches were also prone to trench collapse.

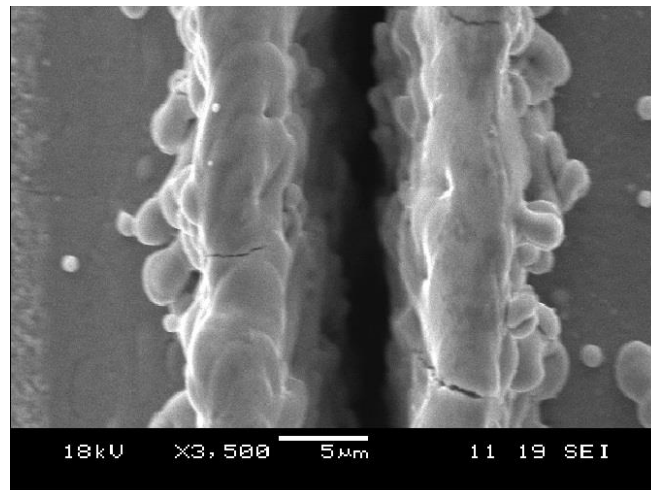


Figure 30 - SEM image of a trench cut in molybdenum as part of testing to improve the laser absorption of the CO<sub>2</sub> surface. The lip at the edge of the trench is visible. This is formed from displaced material from the trench.

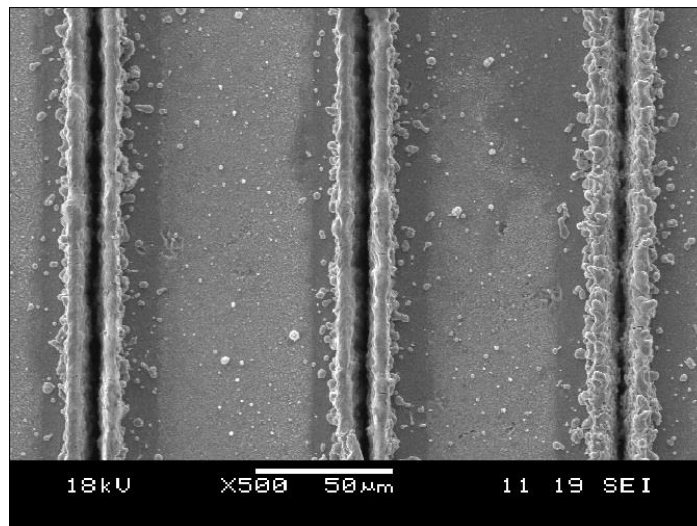


Figure 31 - SEM image of a series of trenches cut in molybdenum. Left most is trench 17, centre is trench 18 and right most is trench 19.

The laser was usually set to perform 5 passes on each trench. The effect of a low number of passes is seen in Figure 31, sample 19. The trench is visibly less deep and the trench edges are not smoothly defined.

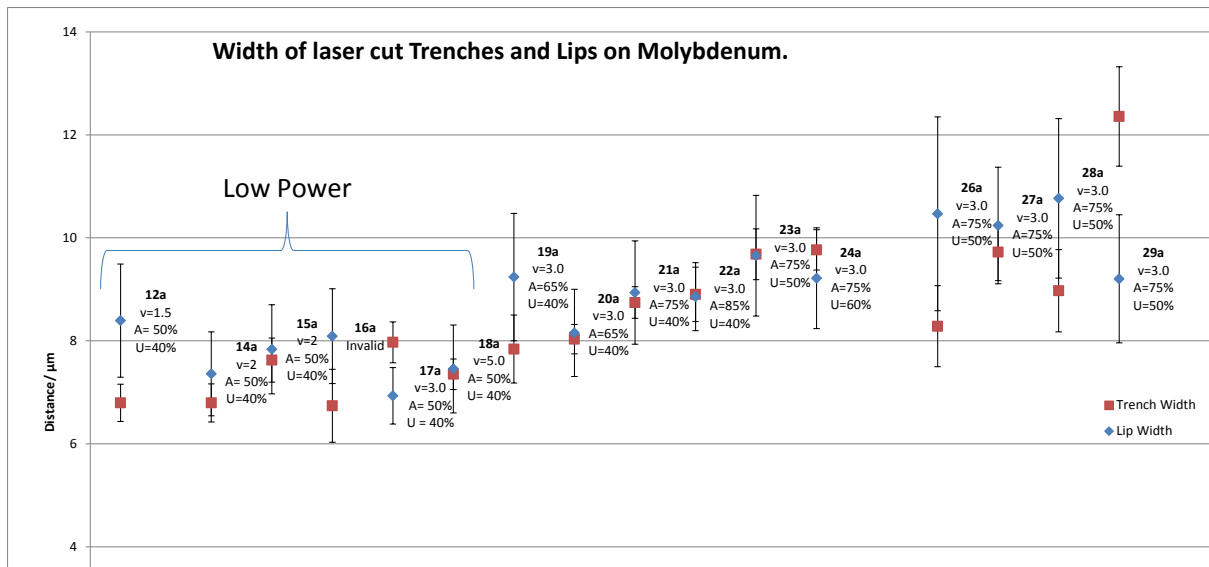


Figure 32 - Width of laser cut trenches in molybdenum as a function of milling parameters. The measurements are taken as an average of individual measurements of the trench/ lip width. Errors are taken as a standard

In Figure 32, it is possible to see that at low powers and high speeds, the width of the trenches was closest to the desired 6µm. These trenches also produced minimal lips which is preferable. The trenches are cut in close proximity in the grating so it is best to have minimal spill over/lip..

With the optimal tested parameters a grating was made by creating a series of the 6µm wide trenches with 4µm space between each trench for a total periodicity of 10µm as in Figure 29. This is the closest periodicity that the laser cutter could manufacture to the 10.6µm laser wavelength. The total dimension of the molybdenum grating was 10mmx10mm with a thickness of 300µm.

### 4.3 Heating Tests

The temperature was calibrated with a thermocouple which measured temperature at the centre of the sample (thermionic cathode). The samples were all thoroughly sonicated for five minute cycles and cleaned using acetone to minimise contamination on the samples before heating.

The power of the laser was ramped up incrementally starting at 0% with increments of 5% power up until the maximum power, 95%. The aim was to evaluate the energy absorption of each sample and determine which could absorb the most energy and provide the best temperature range for thermionic testing.

#### Heating test specimens

- Sample A – BDD (H –terminated, Li Diffused)
- Sample B – Molybdenum
- Sample C - Molybdenum with grating
- Sample D - Molybdenum with 2 micron grown BDD film
- Sample E - BDD + Molybdenum with 2 micron grown BDD film

At about 350°C degassing of contaminants from diamond was commonly observed. At this point the pressure inside the vacuum chamber increased. .

At cathode temperatures past 400°C, hotspots could be observed on the absorber side of the cathode surface. The occurrence of these hotspots is presumed to be contaminant organic species burning off from the surface.

#### 4.4 Thermionic Measurements

Current output from the thermionic sample is measured.

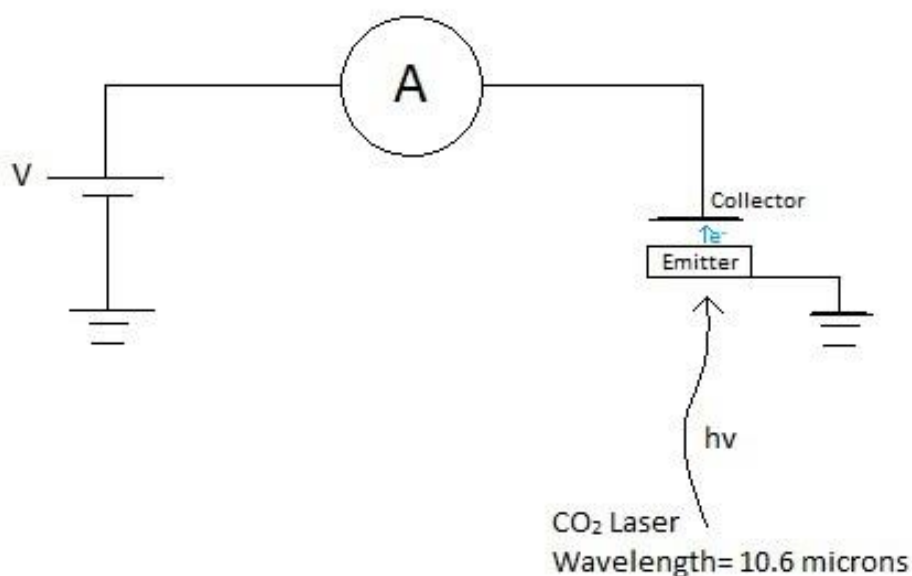


Figure 33 - Circuit diagram of the thermionic setup.

The voltage applied was 25V. The distance between collector and emitter was 2mm. Temperature was measured using a thermocouple placed on the emitting side of the cathode.

The TEC anode and cathode were kept under vacuum at pressures between  $1 \times 10^{-6}$  and  $1 \times 10^{-7}$  Torr. This was to ensure minimal interaction of the cathode emitted electrons with particles before they reached the collector.

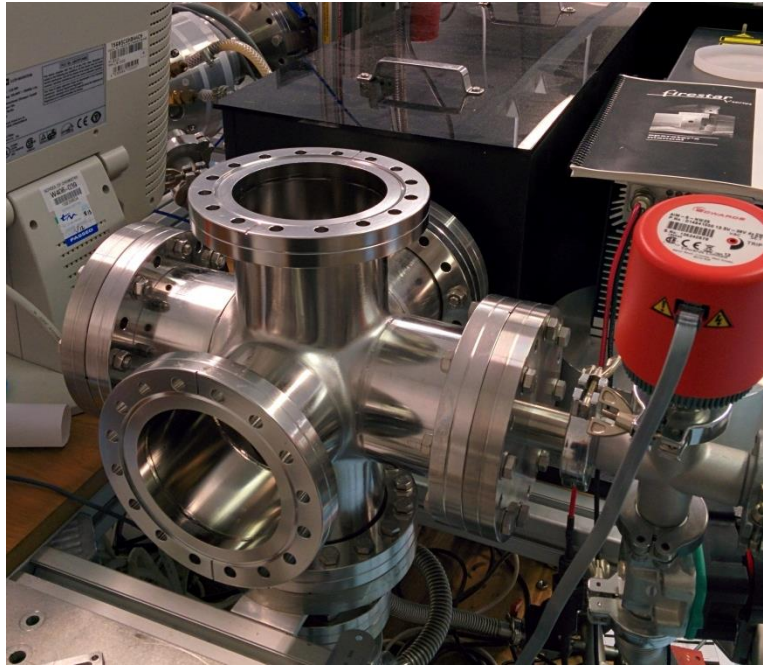


Figure 34 - The vacuum chamber used for the thermionic emission tests at Bristol University Diamond Laboratory

#### 4.5 Results and Discussion

Sample	Material(s)	Max Temperature/ °C	Max Thermionic Emission/ $\mu\text{A cm}^{-2}$
A	BDD (H-terminated, Li Diffused)	799±5	22.2±0.05
B	Molybdenum (Bare)	220±5	N/A
C	Molybdenum with grating	633±5	N/A
D	Molybdenum with 2 micron grown BDD film	681±5	N/A
E	BDD + Molybdenum with 2 micron grown BDD film.	535±5	0.09±0.05
F	BDD (H-terminated)	N/A	11.2±0.05

Table 3 - Table displaying results of heating tests and thermionic emission test with the different samples. Errors displayed for temperature are based on the average fluctuation of temperature over a 1 minute time frame. The errors displayed for current are based on half of the precision of the ammeter.

The absorption of the Mo sample was shown to be improved as the maximum temperature increased from 220°C to 633°C due to the milled grating on the Mo surface. The improvement to Mo absorption was bested by the 2 micron BDD film sample which reached 681°C.

The final grating production ended up with poor trench definition and a visible orange oxide tinge to the surface. It may be possible to reach a higher temperature using the Mo grating by further improving the clarity of the trenches cut. The Bristol University diamond lab laser may be incapable of achieving the required quality of grating due to spill over of extracted material and the cracking

caused in the Mo due to thermal stress. For future gratings, it may be advantageous to use a laser cutter with a smaller beam diameter, used at lower power for an improved precision cut.

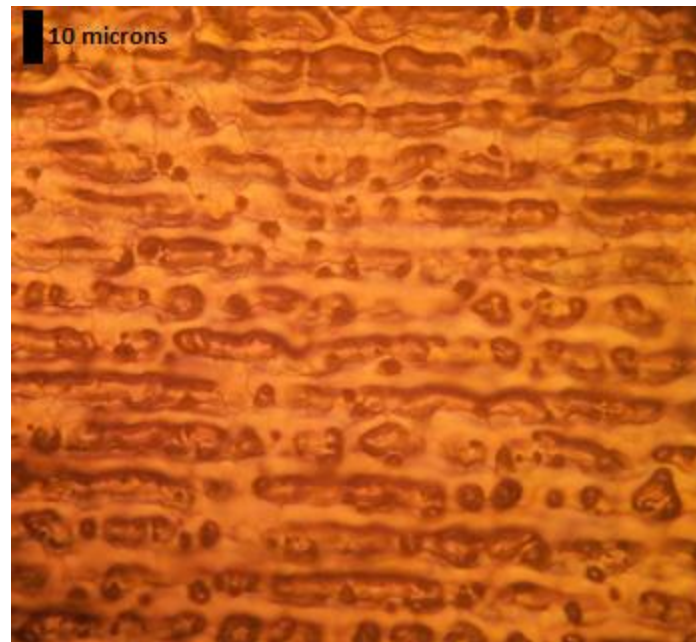


Figure 35 – An optical microscope image of a molybdenum grating with 6 micron wide trenches each separated by a 4 micron gap. The usually grey molybdenum surface has turned a orange/white oxide colour. Trenches are visible but of poor quality and surface cracks can be observed. Despite this, the Mo grating did improve absorption of 10.6 micron wavelength radiation.

The BDD diamond did absorb well and reached the highest temperature of 797°C. This high absorption may be due to the high absorption of boron doped diamond due to the infrared active transition from the ground state to the first excited state of the bound hole as discussed in 3.4.

The Mo with a grown BDD film did reach 681°C however when the Mo piece was clamped with a H-terminated BDD cathode, the heat transfer between the Mo and the diamond was poor. Sample E for this reason did not reach high enough temperatures to perform any significant amount of thermionic emission. The coupling between the Mo and the BDD in any setup where the Mo is used as an absorber was always tricky as it is difficult to attain full contact between the Mo and the diamond. Ideally, diamond would be grown on both sides of the Mo, allowing for maximum contact and maximum transfer of phonons from Mo to diamond.

## Thermionic Emission of H-terminated Freestanding Diamond (Li diffused and without Li)

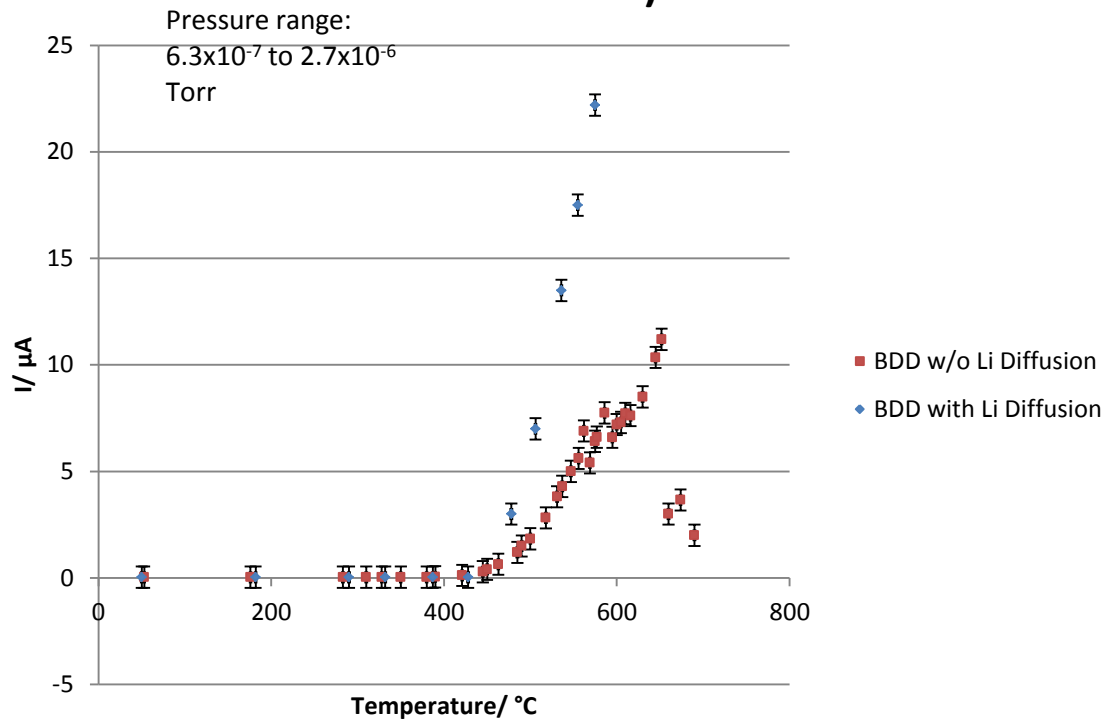


Figure 36 - Emission from H-terminated Li diffused sample A and H-terminated sample F. Freestanding BDD shows emission from around 400°C and a sudden drop in emission levels at 650°C due to hydrogen desorption.

Figure 36 shows BDD with a H-termination emitting. The original BDD diamond sample (sample A) was taken past 650°C, the point at which the H-termination desorbs. The sample was then re-terminated with hydrogen but not lithium diffused (sample F). The thermionic emission results for the sample with no lithium diffusion gave a far lower peak current, showing that the Li diffusion does improve the thermionic emission of H-terminated BDD. The decline in emission at 650°C is due to hydrogen desorption and thus the degradation of the NEA surface.

The emission peaks of 22.2 μA (sample A) and 11.2 μA (sample F) are somewhat difficult to compare to literature values due to the scarcity of results in this area and the difficulty of replicating the exact conditions used for other studies to make fair comparisons. Robinson [32], who publishes some data on the thermionic emission of H-terminated boron doped diamond films does not give comparable data as his measured intensities are in arbitrary units (see Figure 15). Koeck [27] publishes data on H-terminated films though the diamond is nitrogen-doped. Koeck reported emission of 45μA (see Figure 16) from the surface which is a similar region to the results that we gathered experimentally however Koeck's experimental conditions, such as applied voltage and anode cathode separation, were different to our own.

The Li-H-diamond emitter shows low stability (650°C) and future work should be carried out using the Bristol University Diamond Group thermionic equipment to test the emission from the theoretically more stable Li-O terminated diamond when such samples become available.

## 4.6 Conclusion

The laser-heated thermionic setup was successfully established. The freestanding BDD had the strongest absorption of the CO<sub>2</sub> laser and reached a temperature of 799±5°C – well into the operational thermionic temperature range. The 10µm periodicity Mo grating did improve absorption and though the grating quality was low the temperature achieved went from 220±5°C with no grating to 633±5°C with grating. A better manufactured grating which has more defined trenches could still increase infrared absorption beyond that of the freestanding BDD.

The Li – H – Diamond sample was shown to emit at 25.0±0.05µA/ cm<sup>-2</sup> at 500°C. The hydrogen termination at the surface was susceptible to desorption at 650°C causing a loss of the NEA surface. Further work should be carried out on Li-O terminated BDD samples using the laser heated thermionic setup. LiO is likely to be able to reach higher temperatures without degradation of the NEA surface.

## 4.7 Acknowledgements

I would like to thank Hugo Andrade, Sarah Halliwell, Zamir Othman, Jan Harwood, Ben Truscott and Neil Fox for their contributions towards this project and their insightful discussion which helped toward the project progress.

## 5 Bibliography

- [1] H. Ibach and H. Luth, "Semiconductors," in *Solid State Physics 4th Edition*, Berlin, Springer-Verlag, 2009, pp. 419-516.
- [2] M. Kuball, *Semiconductors 4th Year Physics Course*, Bristol: University of Bristol, 2014.
- [3] C. Kittel, *Solid State Physics 8th Edition*, Wiley, 2004.
- [4] O. Richardson, "Electron emission from metals as a function of temperature," *Phys. Rev.*, vol. 23, p. 153, 1924.
- [5] S. Dushman, "Electron Emission from Metals as a Function of Temperature," *Phys. Rev.*, vol. 21, p. 623, 1923.
- [6] J. W. Schwede, I. Bargatin, D. C. Riley, B. E. Hardin, S. J. Rosenthal, Y. Sun, F. Schmitt, P. Pianetta, R. T. Howe, Z.-X. Shen and N. A. Melosh, "Photon-Enhanced Thermionic Emission for Solar Concentrator Systems," *Nature Materials*, vol. 9, 2010.
- [7] G. N. Hatsopoulos and J. Kaye, "Measured Thermal Efficiencies of a Diode Configuration of a Thermo Electron Engine," *Journal of Applied Physics*, vol. 29, p. 1124, 1958.
- [8] F. A. Koeck and R. J. Nemanic, "Emission characterization from nitrogen-doped diamond with respect to energy conversion," *Diamond and Related Materials*, vol. 15, pp. 217-220, 2006.

- [9] R. Bell, *Negative Electron Affinity Devices*, Oxford: Clarendon Press, 1973.
- [10] G. N. Hatsopoulos, *Thermionic Energy Conversion*, Massachusetts: MIT Press, 1973, pp. 219-230.
- [11] T. L. Martin, "Lithium oxygen termination as a negative electron affinity surface on diamond: a computational and photoemission study," University of Bristol, Diamond, 2011.
- [12] J. R. Smith, "Increasing the Efficiency of a Thermionic Engine Using a Negative Electron Affinity Collector," *cond-mat.mtrl-sci*, 2013.
- [13] A. Varpula and M. Prunnila, "Diffusion-Emission Theory of Photon Enhanced Thermionic Emission Solar Energy Harvesters," *Cond-mat.mtrl-sci*, 2012.
- [14] W. Shockley and H. J. Queisser, "Detailed Balance Limit of Efficiency of pn Junction Solar Cell," *Journal of Applied Physics*, vol. 32, p. 510, 1961.
- [15] A. Broers, S. Xia, C. Maloney, X. Zhu and E. Munro, "High Brightness Limited Area Cathodes," *Journal of Vacuum Science and Technology B*, vol. 9, p. 2929, 1991.
- [16] F. Himpsel, J. Knapp, J. VanVechten and D.E. Eastham, "Quantum Photoyield of Diamond (111) - A stable negative affinity emitter," *Physical Review B*, vol. 20, no. 2, pp. 624-627, 1979.
- [17] A. Kraft, "Doped Diamond: A Compact Review on a New, Versatile," *Int. J. Electrochem. Sci.*, 2 (2007) 355 - 385, vol. 2, pp. 355-385, 2007.
- [18] P. W. May, "Diamond Thin Films: a 21st Century Material," *Phil. Trans. R. Soc. Lond. A*, vol. 358, pp. 473-495, 2000.
- [19] P. Partridge, M. Ashfold, P.W. May and E. Nicholson, "The effective chemical vapour deposition rate of diamond," *Journal of Materials Science*, vol. 30, pp. 3973-3982, 1995.
- [20] K. O'Donnell, T. Martin, N. Fox and D. Cherns, "Ab initio investigation of lithium on the diamond C(100) surface," *Physical Review B*, vol. 82, 2010.
- [21] D. Pugh, "Surface States on the (111) surface of diamond," *Physical Review Letters*, vol. 12, no. 14, pp. 390-39, 1964.
- [22] J. P. Goss, R. J. Eyre and P. R. Briddon, "Theoretical models for doping diamond for semiconductor applications," *Phys. Stat. Sol. (B)*, vol. 245, p. 1679, 2008.
- [23] M. Kataoka, C. Zhu, F. A.M. Koeck and R. J. Nemanich, "Thermionic electron emission from nitrogen-doped homoepitaxial diamond," *Diamond and Related Materials*, vol. 19, pp. 110-113, 2010.
- [24] A. D. a. E. Gheeraert, "Hydrogen-boron interactions in p-type diamond," *Physical Review B*, vol.

58, 1998.

- [25] S. Smith and W. Taylor, "Optical Phonon Effects in the Infra-red Spectrum of Acceptor Centres in Semiconducting Diamond," *Proc. Phys. Soc.*, vol. 79, 1962.
- [26] F. Koeck, R. Nemanich, A. Lazea and K. Haenen, "Thermionic electron emission from low work-function phosphorus doped diamond films," *Diamond and Related Materials*, vol. 18, pp. 289-791, 2009.
- [27] F. Koeck, J. Garguilo, B. Brown and R. Nemanich, "Enhanced low-temperature thermionic field emission from surface-treated N-doped diamond films," *Diamond and related materials*, vol. 11, pp. 774-779, 2002.
- [28] M. Z. Othman, P. W. May, N. A. Fox and P. J. Heard, "Incorporation of lithium and nitrogen into CVD diamond thin films," *Diamond and Related Materials*, vol. 44, pp. 1-7, 2014.
- [29] Z. Othman, N. Fox and P. May, "In-situ Incorporation of Lithium and Nitrogen into Diamond Thin Films," *Material Research Society Symp.Proc.*, vol. 1511, 2012.
- [30] P. May, J. Stone, M. Ashfold, K. Hallam, W. Wang and N. Fox, "The effect of diamond surface termination species upon field emission properties," *Diamond and Related Materials*, vol. 7, pp. 671-676, 1998.
- [31] K. Loh, J. Foord, R. Egdell and R. Jackman, "Tuning the electron affinity of CVD diamond with adsorbed caesium and oxygen layers," *Diamond and Related Materials*, vol. 6, pp. 874-878, 1997.
- [32] V. S. Robinson, Y. Show, G. M. Swain, R. G. Refenberger and T. S. Fisher, "Thermionic Emission from surface terminated nanocrystalline diamond," *Diamond and Related Materials*, vol. 15, pp. 1601-1608, 2006.
- [33] A. V. Hamza, G. D. Kubiak and R. H. Stulen, "Hydrogen chemisorption and the structure of the diamond C(100) - (2x1) surface," *Surface Science*, vol. 237, pp. 35-52, 1990.
- [34] H. Andrade and N. Fox, "Use of NanoESCA and Kelvin Probe Force Microscopy to visualise work function changes on diamond thin films terminated with oxygen and lithium mono-layers for thermionic energy conversion".
- [35] S. Lagomarsino and S. Sciortino, "Modeling of the Transport Properties of Diamond Radiation Sensors," *Topics Appl. Phys.*, vol. 100, pp. 303-327, 2006.
- [36] C. Nebel, A. Waltenspiel, M. Stutzmann, M. Paul and L. Schafer, "Persistent photocurrents in CVD diamond," *Diamond and Related Materials*, vol. 9, pp. 404-407, 2000.
- [37] Y. Tzenga, C. Liua and A. Hiratab, "Effects of oxygen and hydrogen on electron field emission from chemical vapor deposited microcrystalline diamond, nanocrystalline diamond and glassy

- carbon coatings," *Diamond and Related Materials*, vol. 12, pp. 456-463, 2003.
- [38] P. Gonon, S. Praver and D. Jamieson, "Photoinduced conductivity changes in polycrystalline diamond films," *Applied Physics Letters*, vol. 68, no. 9, p. 1238, 1996.
- [39] E. E. e. al, "Superconductivity in Diamond," *Nature*, vol. 428, p. 542, 2004.
- [40] H. Umezawa and T. T. e. al, "Advantage on Superconductivity of Heavy Boron Doped (111) Diamond Films," *cond-mat*, 2004.
- [41] University of Reading, "University of Reading Infrared Multilayer Laboratory," 2014. [Online]. Available: <https://www.reading.ac.uk/infrared/>. [Accessed 24 04 2014].
- [42] E. Gheeraert, A. Deneuille and J. Mambou, "Boron-related infra-red absorption in homoepitaxial diamond films," *Diamond and Related Materials*, vol. 7, pp. 1509-1512, 1998.
- [43] P. Kapitza, "Interfacial Thermal Resistance," *J. Phys (USSR)*, vol. 4, 1941.
- [44] S. Murad and I. K. Puri, "Thermal transport across nanoscale solid-fluid interfaces," *Applied Physics Letters*, vol. 92, 2008.
- [45] G. P. Strivastava, *Physics of Phonons*, New York: Taylor and Francis Group, 1990.
- [46] G. Loh, E. Teo and B. Tay, "Compounded effect of vacancy on interfacial thermal transport in diamond graphene nanostructures," *Diamond and Related Materials*, vol. 20, pp. 1137-1142, 2011.
- [47] S. Murad and I. K. Puri, "Thermal transport through superlattice solid-solid interfaces," *Applied Physics Letters*, vol. 95, 2009.
- [48] S. Pillai, K. Catchpole, T. Trupke and M.A.Green, "Surface plasmon enhanced silicon solar cells," *Journal of Applied Physics*, vol. 101, 2007.
- [49] R. Ritchie, E. Arakawa, J. Cowan and R. Hamm, "Surface-plasmon resonance effect in grating diffraction," *Physical Review Letters*, vol. 21, no. 22, 1968.
- [50] P. K. Bachmann, "Diamond Deposition," *Adv. Mater.* 2, vol. No.4, 1990.
- [51] T. Sun, F. Koeck, C. Zhu and R. Nemanich, "Combined visible light photo-emission and low temperature thermionic emission from nitrogen doped diamond films," *Appl. Phys. Lett.*, vol. 99, 2011.
- [52] A. N. Tavkhelidze, "Nanostructured electrodes for thermionic and thermotunnel devices," *Journal of Applied Physics*, vol. 108, 2010.
- [53] P. Partridge, P. May and M. N. R. Ashfold, "Chemical Vapour Deposited Diamond Fibres:

Manufacture and Potential Properties," *Mater. Sci. Technol*, vol. 10, p. 177, 1994.

[54] P. Lurie and J. Wilson, "The Diamond Surface II. Secondary Electron Emission," *Surface Science*, vol. 65, pp. 476-498, 1977.

[55] P. Lurie and J. Wilson, "The Diamond Surface I. The structure of the clean surface and the interaction with gases and metals," *Surface Science*, vol. 65, pp. 453-475, 1977.

[56] J. Robertson, "Electron Affinity of Carbon Systems," *Diamond and Related Materials*, vol. 5, no. 8, pp. 797-801, 1996.

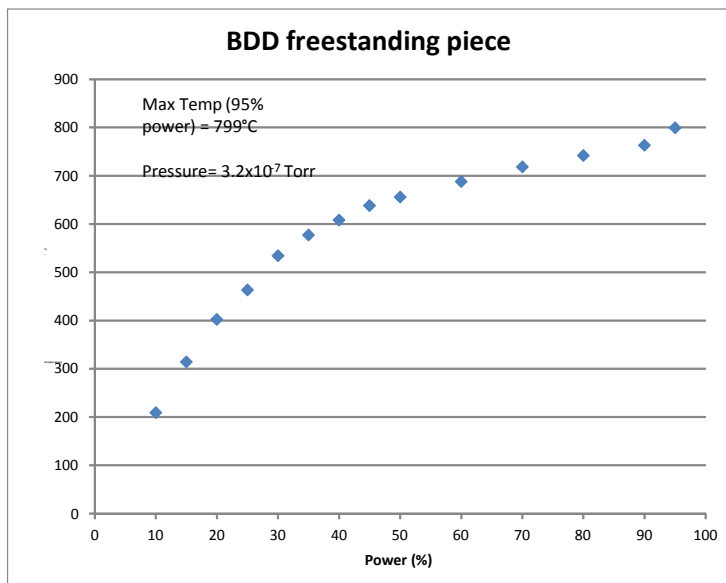
[57] M. Suzuki, T. Ono, N. Sakuma and T. Sakai, "Low-temperature thermionic emission from nitrogen-doped nanocrystalline diamond films on n-type Si grown by MPCVD," *Diamond and Related Materials*, vol. 18, pp. 1274-1277, 2009.

[58] F. Koeck and R. Nemanic, "Sulfur doped nanocrystalline diamond films as field enhancement based thermionic emitters and their role in energy conversion," *Diamond and Related Materials*, vol. 14, pp. 2051-2054, 2005.

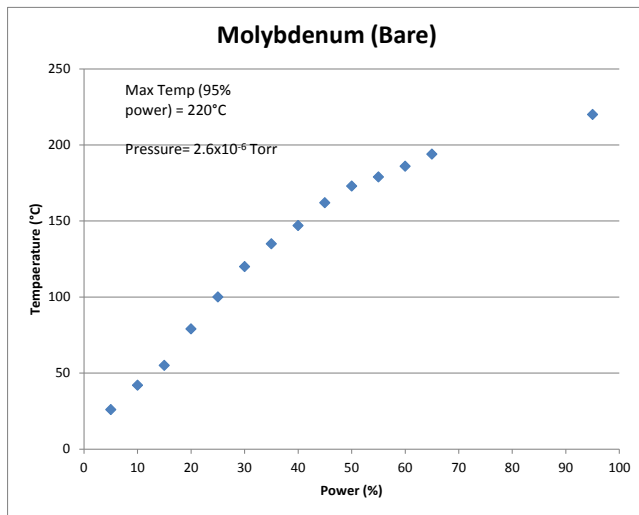
## 6 Appendix

### Heating Test Full Results

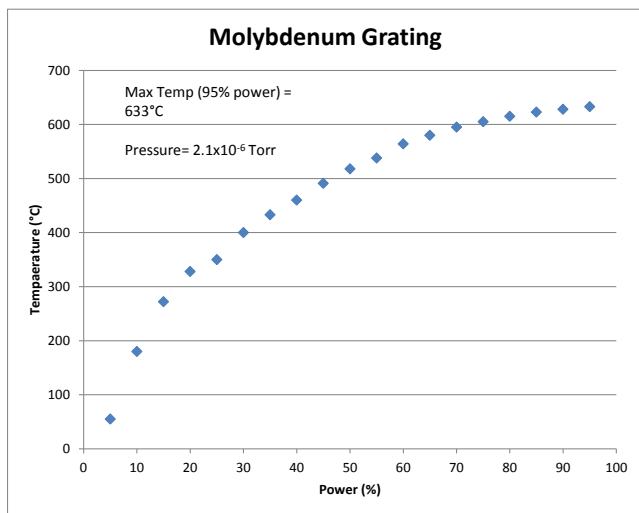
#### Sample A



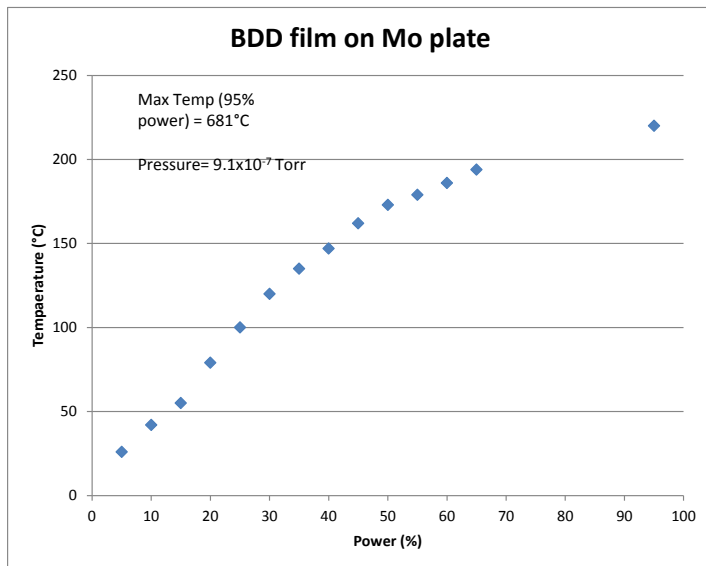
Sample B



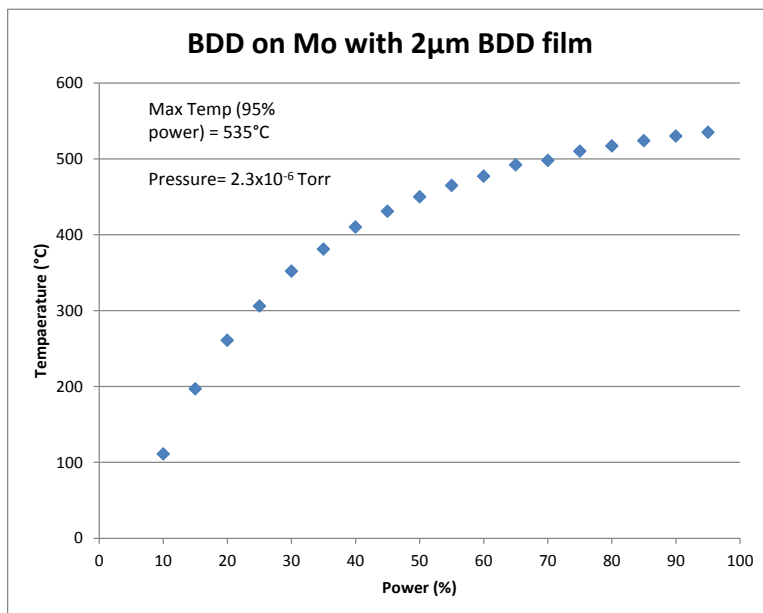
Sample C



Sample D

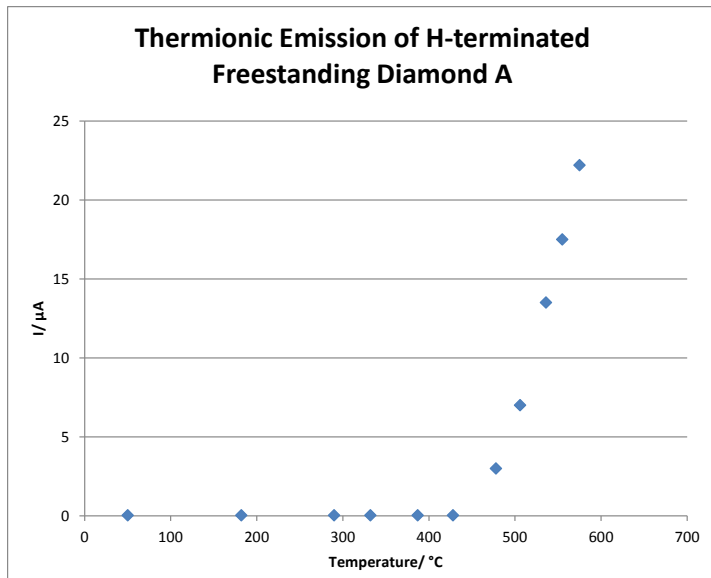


Sample E



Thermionic Emissions

Sample A



Sample F

